



# On Improved Understanding of Airfoil Performance Evaluation Methods at Low Reynolds Numbers

Witold J. F. Koning,<sup>\*</sup> Ethan A. Romander,<sup>†</sup> Haley V. Cummings,<sup>‡</sup> and B. Natalia Perez Perez<sup>§</sup>

NASA Ames Research Center, Moffett Field, California 94035

and

Pieter G. Buning<sup>¶</sup>

NASA Langley Research Center, Hampton, Virginia 23681

<https://doi.org/10.2514/1.C037023>

**Airfoil performance for the Eppler 387 airfoil at low Reynolds number ( $Re_c = 60,000$  to  $460,000$ ) is studied numerically and compared to existing experimental data. Two- and three-dimensional unsteady laminar Navier–Stokes simulations are performed to evaluate the large-scale dynamics of the flow. All cases show laminar separation of the boundary layer followed by the shedding of large coherent vortices resulting in reattachment only observed in the mean flow, referred to as bubble flapping. Integrated aerodynamic coefficients, pressure distributions, and separation–reattachment locations are presented and compared to experimental data. Absolute averaged section lift and drag errors in the range  $Re_c = 100,000$  to  $300,000$  are 5 and 7%, respectively, and good agreement of the pressure distributions is obtained. Laminar separation locations are predicted within 2%-chord, and turbulent reattachment is on average predicted within 5%-chord of the experimental values, which is improved to 3%-chord when updated experimental data are used. The work illustrates that bubble flapping, and the resulting mean airfoil performance, can be analyzed using laminar unsteady Navier–Stokes simulations, and that it does not necessitate external disturbances or three-dimensional instabilities. The shear layer transition over airfoils is found to be dominated by two-dimensional vortex shedding resulting in unsteady reattachment.**

## Nomenclature

$C_f$	=	skin friction coefficient, $\tau_w / (0.5\rho_\infty U_\infty^2)$
$C_p$	=	pressure coefficient, $(p - p_\infty) / (0.5\rho_\infty U_\infty^2)$
$c$	=	chord, m
$c_d$	=	section drag coefficient, $D / (0.5\rho_\infty U_\infty^2 c)$
$c_l$	=	section lift coefficient, $L / (0.5\rho_\infty U_\infty^2 c)$
$D$	=	section aerodynamic drag force, N/m
$L$	=	section aerodynamic lift force, N/m
$M$	=	Mach number
$p$	=	static pressure, N/m <sup>2</sup>
$Re_c$	=	chord-based Reynolds number, $\rho U_\infty c / \mu$
$t$	=	time, $c / U_\infty$
$U_\infty$	=	freestream velocity, m/s
$x$	=	local $x$ coordinate (along chord)
$y$	=	local $y$ coordinate (perpendicular to airfoil surface)
$y^+$	=	dimensionless wall distance
$\alpha$	=	angle of attack, deg
$\mu$	=	dynamic viscosity, N · s/m <sup>2</sup>
$\rho$	=	density, kg/m <sup>3</sup>
$\tau_w$	=	wall shear stress, N/m <sup>2</sup>

## Subscripts

$c$	=	chord-based
$x$	=	separation–reattachment distance
$\infty$	=	freestream condition

Received 6 May 2022; revision received 7 September 2022; accepted for publication 31 January 2023; published online 22 February 2023. This material is declared a work of the U.S. Government and is not subject to copyright protection in the United States. All requests for copying and permission to reprint should be submitted to CCC at [www.copyright.com](http://www.copyright.com); employ the eISSN 1533-3868 to initiate your request. See also AIAA Rights and Permissions [www.aiaa.org/randp](http://www.aiaa.org/randp).

<sup>\*</sup>Aerospace Engineer, Aeromechanics Branch, and Science and Technology Corporation; [witold.koning@nasa.gov](mailto:witold.koning@nasa.gov). Member AIAA.

<sup>†</sup>Aerospace Engineer, Aeromechanics Branch; [ethan.romander@nasa.gov](mailto:ethan.romander@nasa.gov).

<sup>‡</sup>Mechanical Engineer, Aeromechanics Branch; [haley.cummings@nasa.gov](mailto:haley.cummings@nasa.gov).

<sup>§</sup>Aerospace and Mechanical Engineer, Aeromechanics Branch, and Science and Technology Corporation; [natalia.perezperez@nasa.gov](mailto:natalia.perezperez@nasa.gov).

<sup>¶</sup>Aerospace Engineer, Computational AeroSciences Branch; [pieter.g.buning@nasa.gov](mailto:pieter.g.buning@nasa.gov). Associate Fellow AIAA.

## I. Introduction

VARIOUS small-scale unmanned aerial vehicles (UAVs) and micro air vehicles (MAVs) utilize airfoils at low chord-based Reynolds numbers ranging from roughly  $Re_c = 10,000$  to  $Re_c = 500,000$  [1–4]. The inherently low lift-to-drag ratios attainable at low Reynolds numbers make flight challenging compared to more conventional Reynolds numbers [2,4,5]. Efficient airfoil performance is the prerequisite to satisfactory vehicle operation, and the proper understanding of airfoil performance in this Reynolds number regime is therefore of fundamental significance [6–9].

Conventional airfoils at higher Reynolds numbers usually experience laminar–turbulent transition of the boundary layer through growth of convective (viscous type) instabilities, allowing airfoils to reach relatively high lift-to-drag ratios compared to those observed at lower Reynolds numbers. With decreasing Reynolds number, the relative strength of the viscous forces increases compared to the inertial forces, progressively damping disturbances found in the flow and delaying laminar–turbulent transition of the boundary layer. Consequently, the boundary layer on the airfoil upper surface may remain laminar downstream of the point of pressure recovery [10]. The laminar boundary layer can only support a small adverse pressure gradient without separation, compared to a fully turbulent boundary layer [11], and will therefore commonly separate at lower Reynolds numbers. The laminar separated shear layer is susceptible to various flow instabilities that can result in steady flow reattachment at sufficient Reynolds number or low angle of attack, forming a laminar separation bubble (LSB). The net drag is increased due to the pressure drag component caused by laminar separation, despite a possible reduction in friction drag due to the flow reversal in the region of separated flow [12], revealing the primary impediment to low-Reynolds-number airfoil performance [13]. The lift is decreased due to the increased boundary-layer thickness at lower Reynolds numbers (and possible flow separation), although to a lesser extent than the increase in drag coefficient [5,14,15]. The steep deterioration of aerodynamic performance for conventional airfoils starts below roughly  $Re_c = 100,000$  to  $Re_c = 500,000$  [1–3,16] with maximum section lift-to-drag ratios decreasing over one order in magnitude compared to higher-Reynolds-number flows. At lower Reynolds number or higher angles of attack, large-scale flow separation on the airfoil can occur without reattachment, stalling the airfoil.

The stability, transition, and unsteady characteristics of separated shear layers are fundamentally different from those of boundary layers [17]. Tollmien–Schlichting (T-S) waves transferred into the laminar separated shear layer, originating from the boundary layer before separation, can grow exponentially, possibly causing laminar–turbulent transition of the shear layer with resulting steady reattachment (approximately above  $Re_x = 50,000$  [1,3], based on the distance from separation to reattachment) [18–20]. The instability to viscous-type T-S waves is often the primary instability up to the separated flow region, whereas the separated shear layer is subsequently also unstable to the (inviscid) Kelvin–Helmholtz (K-H) instability [21–26], although self-sustained oscillations and other instabilities are also found [27–30,71]. The convectively driven instability to viscous-type T-S waves in the shear layer is susceptible to various flow disturbances through receptivity influences for laminar near-wall flows (e.g., forcing fields such as freestream turbulence and vibrations, or catalysts such as surface non-uniformities) [30]. Below the “critical Reynolds number” [5] (around  $Re_c = 100,000$  to  $Re_c = 500,000$ ) there is evidence that T-S-based laminar–turbulent transition with steady reattachment is unlikely without boundary-layer trips, strong receptivity forcing fields, or other catalysts [1–3,16,23].

In absence of rapid breakdown to turbulence, the reattachment process can be an unsteady phenomenon, referred to as bubble flapping, with large spanwise structures shedding into the turbulent boundary layer [23,31,32]. “Bubble bursting” was first defined as the process through which a short bubble transitions to a long bubble [33]. This is likely the transition from an LSB with relatively steady reattachment to a (time-averaged) unsteady bubble (bubble flapping) and indicates the onset of vortex shedding [21]. The term “bubble bursting” is avoided in this work due to the multiple definitions used since the inception of the term [22]. Crucial parameters determining whether the reattachment process is relatively steady or unsteady (bubble flapping) for airfoils are observed to be the angle of attack, the Reynolds number, and freestream disturbance levels [34].

The inviscid K-H instability occurs in the flow over an airfoil due to the inflectional velocity profile of a separated shear layer, resulting in oscillations that can cause the shear layer to roll-up before the onset of K-H vortices, which can develop downstream, amalgamate, and ultimately cause the formation of large-scale vortex shedding [19,21–23,25,35–39]. Two consecutive vortices can move around each other and merge into a larger vortex by mutual induction under certain conditions [39].

The separated shear layer can recover more energy through entrainment mechanisms, increasing the likelihood of (mean) flow reattachment as a turbulent boundary layer on the airfoil further downstream [2,32,34,40]. The shedding of coherent vortices and resulting spanwise structures is sometimes accredited to the primary instability mechanics of the K-H instability [18,22,23] and is thought to play the dominant role in the separation region, having a large impact on fluctuating forces [36]. Deformation of the spanwise vortical structures results in breakdown to smaller eddies by turbulent diffusion [41,42] and can be responsible for mean flow reattachment [41]. The airfoil surface is thought to provide a stabilizing effect to large scale structures, and amplification of the oscillations at low Reynolds numbers might not be fast enough to cause full transition to small-scale turbulence [23,43]. The coherent structures are observed to persist throughout the reattached turbulent boundary layer (with smaller scales superimposed on the larger structures) [22,44], and can play a crucial role in convecting three-dimensional (3D) vorticity further downstream, thereby influencing (and delaying) the observed transition behavior [45,46]. Other work, however, primarily found rapid breakdown to small-scale turbulence [47].

As the Reynolds number is reduced below the critical Reynolds number, the likelihood of viscous T-S based laminar–turbulent transition decreases, and coherent structures are found to be more prominent in the separated flow region [23,34,48]. The role of small-scale turbulence might be only minor in this case [19,23,44,48,49], and experiments showed that the small-scale oscillations and the large-scale vortex shedding are independent and uncorrelated [50].

Roshko [44] describes turbulent mixing layers (around  $Re_c \approx 100,000$ ) and states: “The mean flow is controlled by the large, organ-

ized structures which, it may be seen, are not affected by the small-scale turbulence appearing at the higher values of Reynolds number.” Roshko [44] further notes that the large-scale eddies are responsible for the gross (mean) flow characteristics and notes that “further ‘turbulization’ by smaller eddies is merely a stage in the dissipation of the energy that has been extracted from the mean flow” [44].

Jones et al. [28] show for airfoils that, at sufficiently low disturbance levels, absolute instability of the two-dimensional (2D) vortex shedding occurs and the separation and reattachment locations are fixed: “[I]n the absence of convectively driven transition within the shear layer, transition will take place by absolute instability of the two-dimensional vortex shedding in a manner not predicted by linear stability analysis of the time-averaged flow field” [28]. This can have important consequences on the modeling requirements for such flows and serves as a main motivation for the present work.

The goal of this paper is to computationally examine low-Reynolds-number airfoil performance at low disturbance levels and demonstrate that unsteady laminar Navier–Stokes (NS) simulations can account for the primary flow structures, larger vortical dynamics, and mean airfoil performance at such conditions. The experimental results for the Eppler 387 airfoil in the Langley Low-Turbulence Pressure Tunnel (LTPT) at NASA Langley Research Center are replicated for the Reynolds number range reported (ranging from  $Re_c = 60,000$  to  $Re_c = 460,000$ ) [51]. Wherever available, other experimental sources are included as well. Unsteady laminar NS simulations are compared to experimental airfoil performance, and attention is given to differences between 2D and 3D simulations.

In the next section a brief overview of the experimental work in Ref. [51] at NASA Langley Research Center is given. The numerical approach will be discussed afterward, including a validation effort comparing the present numerical approach to published direct numerical simulation (DNS) results. Results include mean integrated aerodynamic coefficients, pressure distributions, and separation–reattachment locations, all compared to experimental results. The discussion considers the importance of spanwise flow, the modeling of flapping bubbles, the origin of the oil accumulation in the flow visualizations, and the dual flow state observed at  $Re_c = 60,000$ , followed by the conclusions.

## II. Experimental Work on the Eppler 387

The Eppler 387 lends itself well to a computational investigation of low-Reynolds-number airfoil performance due to the large amount of experimental data available. Experimental results in the present work are gathered from the LTPT at NASA Langley Research Center [51], the Model Wind Tunnel at Stuttgart [52], the Low-Turbulence Tunnel at the Delft University of Technology [53], the Subsonic Aerodynamics Lab  $3 \times 4$  ft wind tunnel at the University of Illinois at Urbana-Champaign (UIUC) [54,55], and the Notre Dame Aerospace Laboratory low-speed wind tunnel at the University of Notre Dame [56]. Table 1 summarizes these experiments, including the approximate freestream turbulence levels. The primary reference for the

**Table 1** Freestream turbulence levels for experimental results from referenced facilities

Facility	Reynolds number, $Re_c$	Freestream turbulence level, FSTL, %
Low turbulence pressure tunnel (NASA Langley), Ref. [51]	60,000	0.16–0.20
	100,000	0.05–0.16
	200,000	0.05
	300,000	0.05
	460,000	0.05
Model wind tunnel (Stuttgart), Ref. [52]	—	~0.03
Low-turbulence tunnel (Delft University of Technology), Ref. [53]	—	~0.08
University of Illinois at Urbana-Champaign, Refs. [54,55]	—	<0.1
Low-speed wind tunnel (University of Notre Dame), Ref. [56]	NA	NA

Eppler 387 performance in this report is the LTPT test due to its vast number of published runs, repeated data points, and tabulated results (for integrated aerodynamic forces, pressure distributions, and separation–reattachment locations). The following section describes the basics of the experiment in Ref. [51] conducted in the LTPT.

The LTPT is a closed-circuit, continuous-flow wind tunnel with variable operating pressure. The tests at NASA Langley were conducted over a Reynolds number range from  $Re_c = 60,000$  to  $Re_c = 460,000$  with a Mach number ranging from  $M = 0.03$  to  $M = 0.13$ . The sectional lift and pitching moment data were obtained by integration of pressure measurements over the centerline of the airfoil model, and the section drag coefficient was obtained using wake surveys. Laminar separation and turbulent reattachment locations were obtained from oil-flow visualizations. Tests were also performed with a strip of turbulator tape at one of the investigated Reynolds numbers, but these results are not examined in the present work. Standard low-speed wind tunnel boundary corrections are applied to the presented data, and further discussed in Ref. [51].

For all comparisons to experiments, all available experimental data points (both from the LTPT tests, and other references) are presented to provide the reader with an idea of the scatter in the available test data.

### III. Numerical Approach

Airfoil performance for all simulations is obtained using structured grids and solved using the implicit, compressible NS solver OVERFLOW 2.2o [57,58]. Inviscid fluxes are computed using the Harten, Lax, and van Leer contact (HLLC) flux scheme with a fifth-order WENOM upwind reconstruction approach for high spatial accuracy with low numerical dissipation [59]. Viscous fluxes are computed using second-order central differencing, as are grid metric terms. Time advance uses a standard second-order backward differencing scheme (BDF2), with the dual time-stepping approach as described in Refs. [60–62]. All simulations use low-Mach preconditioning (LMP) with the dual time-stepping methodology in OVERFLOW to improve spatial accuracy and convergence while preserving time accuracy [61,62].

As the results can be sensitive to the choice of preconditioning parameters, all simulations comparing to experiments are set up identically (all simulations are run at equal freestream Mach number  $M = 0.03$  and equal LMP “tuning parameters” such as reference speed and characteristic length of the flowfield). The study aims to keep the Courant–Friedrichs–Lewy (CFL) condition in the separated flow region at unity for efficiency, which in turn determines the physical time step for the simulation.

Unsteady NS (UNS) simulations are more computationally demanding than their steady counterpart but allow for the investigation of differences between the mean flow and time-accurate flow. Steady simulations might not be able to converge in the first place with large unsteady features [63,64]. Subiterations are continued until three orders of subiteration convergence are achieved, after an initial coarse set of  $t = 10$  flow passes are simulated to remove initial transients.

A turbulence model is not utilized in the present work, thereby omitting any attempt at modeling the Reynolds stresses and resulting in laminar UNS simulations throughout. In a similar vein, Spalart [64] describes unsteady Reynolds-averaged Navier–Stokes (unsteady RANS, or URANS) flowfields as “periodic in time and smoother than the true turbulent field but representative in some sense, so that its inviscid dynamics mirror the large-scale dynamics of the true flow” [64]. It is these inviscid dynamics and resultant large-scale coherent structures that are hypothesized herein to be dominant for the bubble behavior and thus for airfoil performance. Furthermore, by not utilizing a turbulence model (responsible for approximating the incoherent motion), it is possible to investigate causal contributions of the larger temporal and spatial scales to the flowfield in absence of any effect of small-scale turbulence. It is the computational advantage of running laminar UNS versus turbulent URANS (or higher-fidelity approaches) that is deemed worthwhile to explore in the present work, which could be especially beneficial in earlier stages of aerodynamic design of low-Reynolds-number airfoils.

The experimental data report does not disclose enough information to fully determine the experimental operating conditions for the

simulation [51]. Therefore, while the Reynolds number and Mach number are matched, International Standard Atmosphere (ISA) conditions at sea level are used for all simulation results presented in this report.

All airfoil surfaces are subjected to a no-slip adiabatic boundary condition, the far-field boundaries are modeled using a freestream characteristic boundary condition, and the spanwise boundary conditions (in the case of 3D simulations) are modeled using a pure extrapolation (outflow) boundary condition. The spanwise boundary condition choice is arbitrary [64], but the outflow boundary condition is preferred over a spanwise periodic boundary condition to avoid forcing periodicity over a relatively short span, especially when only sectional performance at the centerline is sought (and expanding the spanwise distance comes at considerable increase in computational cost).

Integrated aerodynamic forces and pressure distributions are obtained over the *centerline* of the model in 3D computations (instead of using span-averaged values) to replicate the experimental setup used in the LTPT experiments. The lift forces in the LTPT are obtained by integration of the pressure-only measurements over the airfoil surface. The differences with numerical integration of the total aerodynamic forces (pressure and friction) over the same area were confirmed to be negligible.

#### A. Eppler 387 Geometry and Structured Grid

The Eppler 387 airfoil coordinates were obtained from Ref. [51] and interpolated to yield a high-density set of coordinates. The Eppler 387 airfoil, shown in Fig. 1, was modified to use a 0.25%*c*-thick round trailing edge (TE) instead of an unrealistic sharp edge to improve grid quality, which was blended into the Eppler 387 coordinates at  $x/c \approx 0.95$  (this is comparable to the modifications performed to the experimental model in Ref. [51]).

Both 2D and 3D structured grids are employed for the airfoil studies. Initially, a coarse overset grid with dynamic (near-body) adaptive mesh refinement (AMR) [65] was pursued to increase computational efficiency. However, this was later abandoned in favor of a fine single fixed grid due to difficulty in choosing a single representative grid cell size in the unsteady region of the flow preferred for the LMP approach.

The grids were generated using Chimera Grid Tools 2.2 (CGT) [66], and the gridding guidelines from the AIAA CFD High Lift Prediction Workshop are used where applicable [67]. The 2D grid size is based on the grid resolution study included in Refs. [68,69], resulting in an O-grid with chordwise spacing at the leading edge and TE set to 0.001%*c* and 0.01%*c*, respectively. The number of cells over the TE is monitored to ensure adequate gridding. The maximum chordwise separation was fixed at 0.5%*c* to provide a reasonably uniform chordwise grid spacing in the predominant region of unsteady separated flow, aiding the efficacy of the LMP approach.

The viscous wall spacing is estimated for the first point of the airfoil surface at 10%*c* and kept at  $y^+ < 1$  for all Reynolds numbers studied. The initial wall spacing layer contains five layers of constant cell spacing normal to the viscous walls. The cell stretching ratio (SR) for the normal and tangential/chordwise layers is kept at 10%, and the far field is located at 20*c* for all grids. The number of cells normal to the surface is obtained from the target stretching ratios. For 3D grids, the 2D grid was repeated in the spanwise direction over constant

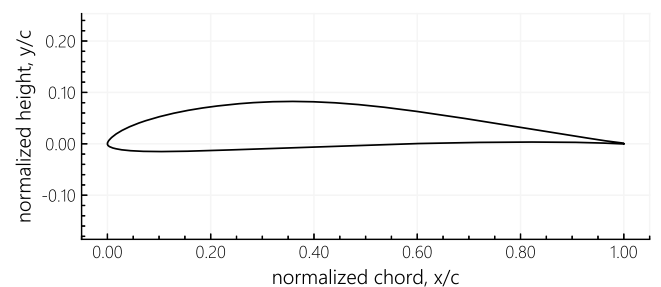


Fig. 1 The Eppler 387 airfoil profile.

intervals of  $0.5\%c$ . The spanwise spacing was kept uniform and identical to the maximum chordwise separation of  $0.5\%c$  to approach uniformly sized cells in the predominant separation region. A test was performed at  $Re_c = 60,000$  and an angle of  $\alpha = 6.5^\circ$ , confirming virtually undistinguishable centerline pressure distributions between a span close to  $0.5c$  and  $1.0c$ ; the former was chosen to conserve computational expense. The 3D grids are referred to as quasi 3D (q3D) because of their limited span. The O-grids on the airfoil have 1329-by-145-by-113 grid points in the chord, normal, and spanwise directions, respectively.

## B. Validation of Numerical Approach

To validate the numerical approach, results at  $Re_c = 60,000$ ,  $M = 0.0732$ , and  $\alpha = 6.0^\circ$  were compared to DNS results for the Eppler 387 airfoil in Ref. [70]. This work was selected because it published both 2D and 3D analyses, as well as the pressure and skin-friction distributions over the airfoil. As will be seen in the following (sub)sections, the numerical approach used is validated for 2D simulations by the excellent agreement to DNS results of Ref. [70]. Comparison with the corresponding 3D case presents some issues, however, which are discussed below. The validity of the 3D approach is borne out by both the quality of agreement with experiment shown in the Results section as well as the analysis of the  $Re_c = 60,000$ ,  $\alpha = 6.0^\circ$  validation case shown below coupled with discussion and results shown in Fig. 11.

### 1. Two-Dimensional Time-Accurate Comparison

Figure 2 shows the time-accurate vorticity magnitude in OVERFLOW for the 2D case. The flowfield clearly shows the separated shear layer and subsequent shedding of large-scale vortices.

The unsteady laminar OVERFLOW results are presented in Figs. 3 and 4, showing the instantaneous pressure coefficient and skin friction coefficient, respectively. The chordwise locations of the pressure and skin friction peaks were chosen to approximately match those

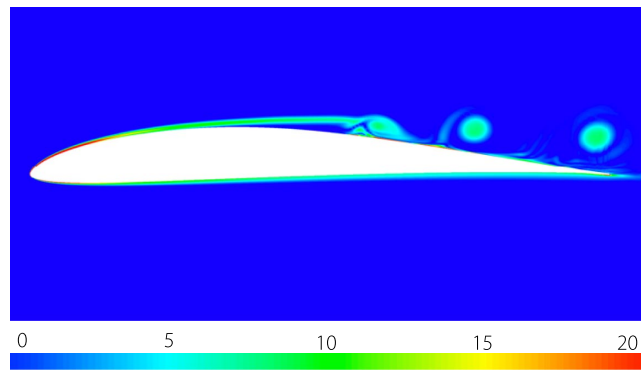


Fig. 2 Instantaneous vorticity magnitude (2D, nondimensional).

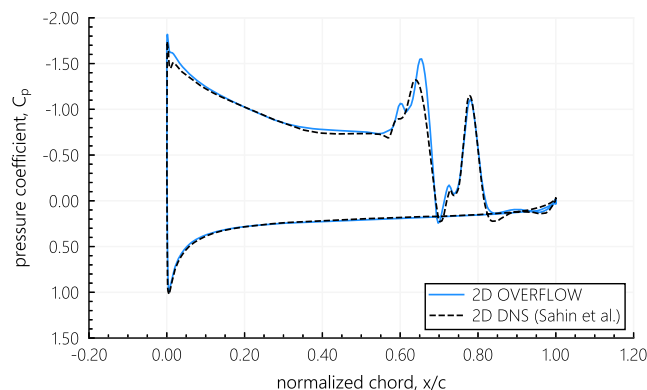


Fig. 3 Instantaneous comparison of 2D pressure coefficient to DNS from Ref. [70].

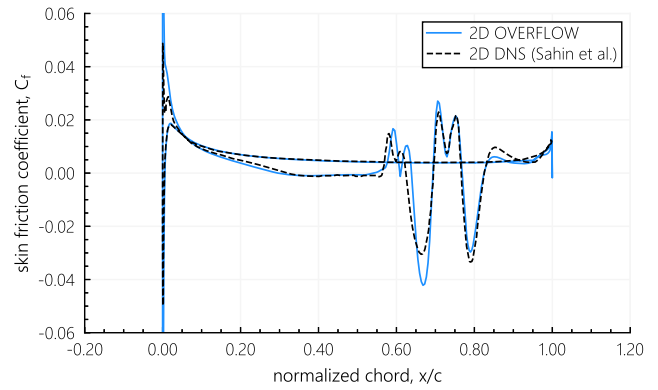


Fig. 4 Instantaneous comparison of 2D skin friction coefficient to DNS from Ref. [70].

found in the results of Ref. [70], thereby allowing a qualitative comparison of the time-accurate results.

The shedding of vortices can be clearly observed in the pressure distribution resulting in increased lift peaks. The skin friction sign at the increased lift peaks is negative, reducing friction drag slightly.

### 2. Two-Dimensional Time-Averaged Comparison

The simulation results are averaged over  $t = 40$  flow passes. Both the pressure coefficient and skin friction coefficient over the airfoil are presented in Figs. 5 and 6, respectively. The mean section lift coefficient in Ref. [70] is  $c_l = 0.9752$ , compared to  $c_l = 0.9844$  in the present work. The mean section drag coefficient in Ref. [70] is  $c_d = 0.0425$ , compared to  $c_d = 0.0428$  in the present work. The differences in section lift and drag coefficient are less than 1%. Both time-accurate and mean flow comparison show good agreement in 2D simulations.

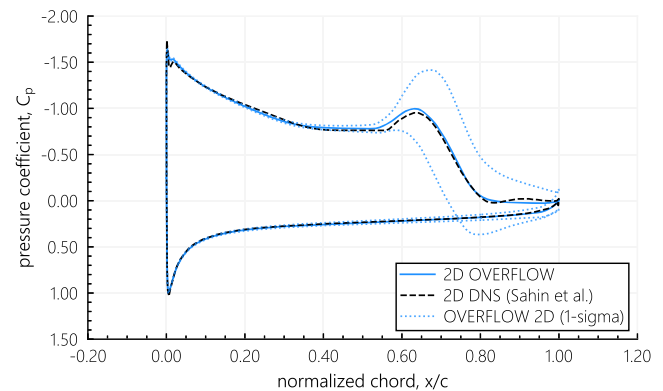


Fig. 5 Time-averaged comparison of 2D pressure coefficient to DNS from Ref. [70].

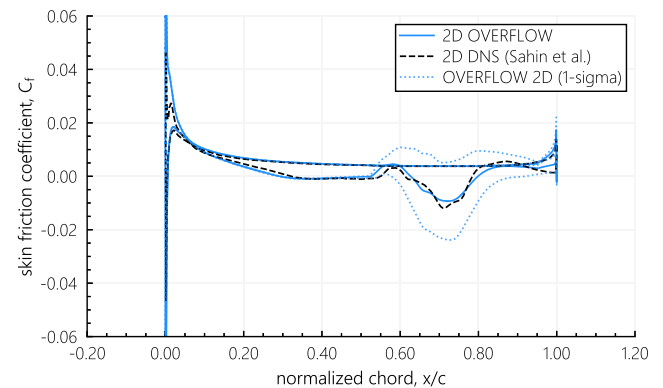


Fig. 6 Time-averaged comparison of 2D skin friction coefficient to DNS from Ref. [70].

### 3. Quasi-3D Time-Averaged Comparison

Figure 7 shows the center plane of the time-accurate vorticity magnitude for the q3D simulation, showing the clear influence of the third dimension on the unsteady flow.

The time-averaged comparison of the 3D simulation is shown in Fig. 8. The integrated forces are less periodic compared to the 2D simulation and show large random variations over time. The q3D simulation almost predicts reattachment of the mean flow, whereas the DNS simulations in Ref. [70] show laminar separation. McGhee and Walker [51] report that, for the experiments at  $Re_c = 60,000$ , approximately between  $2.5^\circ < \alpha < 7.0^\circ$ , two flow states exist simultaneously (laminar separation with and without turbulent reattachment), which are observed repeatedly and recurring for all operating conditions (independent of Mach number, corresponding freestream turbulence intensity [FSTI] levels at  $Re_c = 60,000$ , or hysteresis effects). The two states can be clearly seen later in the force data (shown in Fig. 11). Unfortunately, only the laminar separation (without reattachment) data were recorded for  $\alpha = 6.0^\circ$  (both pressure distribution and integrated aerodynamic forces), making it hard to cast judgement on the simulation results.

Table 2 shows the mean sectional lift and drag for 2D and 3D simulations in OVERFLOW and in Ref. [70], compared to the LTPT experimental results.

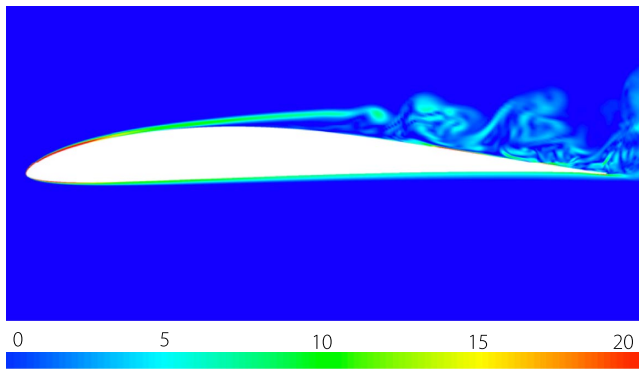


Fig. 7 Instantaneous vorticity magnitude (midspan, q3D, nondimensional).

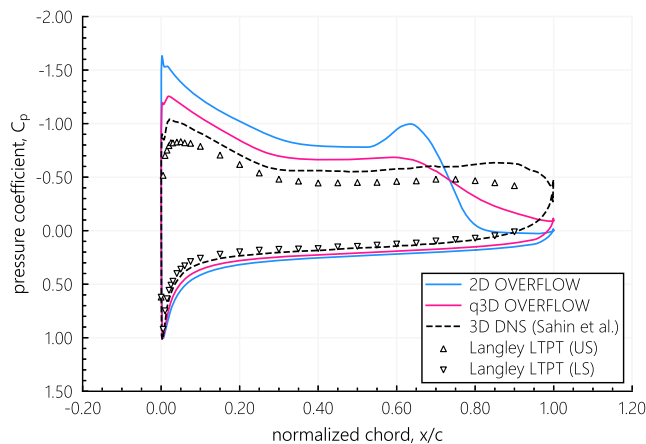


Fig. 8 Time-averaged comparison of q3D results to DNS results from Ref. [70].

Table 2 Sectional lift and drag for all validation cases

Source	Section lift, $c_l$	Section drag, $c_d$
OVERFLOW (2D)	0.984	0.0428
DNS (2D, Ref. [70])	0.975	0.0425
OVERFLOW (q3D)	0.865	0.0517
DNS (3D, Ref. [70])	0.813	0.0772
LTPT (LS)	0.661	0.0639

The sectional lift and drag errors are around  $\sim 20\%$  for both 3D numerical approaches, compared to LTPT data. In light of the good comparison of the 2D cases between the two numerical approaches, and the particular issues with this operating condition, as shown in Ref. [51], it was decided to pursue the current work. The dual flow state is investigated separately in the discussion.

## IV. Results

This section presents the results of the simulations grouped into mean integrated aerodynamic forces, mean pressure distribution, and separation–reattachment locations. Due to their higher computational cost, q3D cases for some conditions are run at coarser angle of attack intervals.

### A. Mean Integrated Aerodynamic Forces

Mean integrated aerodynamic forces are obtained through integration over the centerline of the airfoils: a strip with a width of  $0.01c$  for q3D cases, or integration over the airfoil contour for 2D cases. The aerodynamic forces are obtained by integration of the pressure and shear stress over the airfoil. The experimental lift is obtained through integration of the pressure over the airfoil centerline and the drag is obtained from the wake rake survey [51].

At low Reynolds numbers the vortex shedding can cause large fluctuations of the forces, which do not always occur at regular intervals. Therefore, the simulation results are presented as boxplots, showing the median and confidence interval values to give a representation of their variation in time. The lift and drag curves for  $Re_c = 100,000$  are shown in Figs. 9 and 10, respectively. The boxplots for 2D simulations are shifted by  $+0.30$  deg to not overlap with the q3D boxplots.

Lift and drag follow the experimental trend well, especially considering the variation in measurements between all experimental sources. As expected, upon stall (approximately at  $\alpha > 7.5^\circ$ ), the drag values start to diverge from experimental values due to increases in flow separation. Two-dimensional simulation results, unaffected by end-effects and the spanwise dimension, show a similar trend to q3D simulation results, although at a positive offset in sectional drag. The reduction in section drag with increasing angle of attack (between around  $\alpha = 4^\circ$  to  $\alpha = 8^\circ$ ) is because of a progressively shortening mean bubble length (as shown later).

The dramatic effect of the “dual flow state” at  $Re_c = 60,000$  is shown in Fig. 11, showing that both laminar separation (corresponding to high section drag values) and turbulent reattachment (corresponding to low section drag values) are occurring for all LTPT runs,

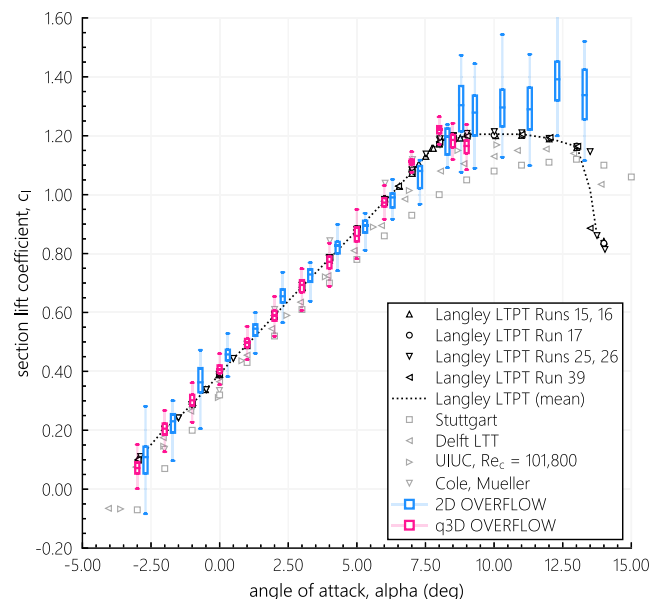
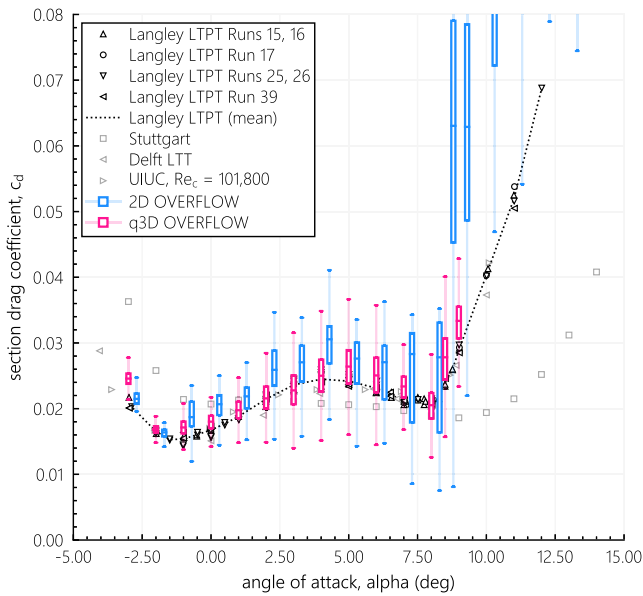
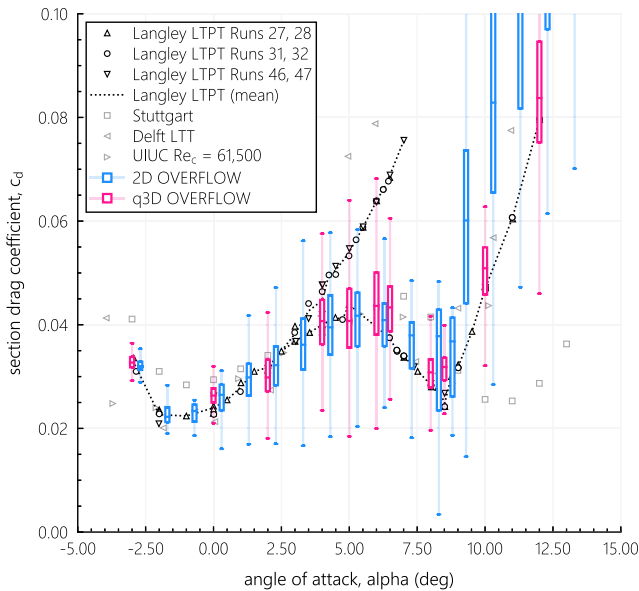


Fig. 9 Section lift for  $Re_c = 100,000$  compared to available experimental data from Refs. [51–54,56].



**Fig. 10** Section drag for  $Re_c = 100,000$  compared to available experimental data from Refs. [51–54].



**Fig. 11** Section drag for  $Re_c = 60,000$  compared to available experimental data from Refs. [51–54].

and therefore independent of Mach number and FSTI. The mean LTPT data are divided into the two distinct groups.

McGhee and Walker [51] also note that no hysteresis loops occurred during testing but that for  $Re_c < 100,000$  the unsteady wakes caused considerable difficulties in obtaining reliable drag numbers. No separation–reattachment data is presented in Ref. [51] for  $Re_c < 100,000$ , presumably due to the inconsistent or nonexistent reattachment behavior (and long runtimes required to establish the oil pattern [55]). Simulations consistently predict flow reattachment (indicative of the lower of the two experimental mean drag trajectories in Fig. 11), but with large unsteady features in the flow, as was observed experimentally.

Drag predictions at  $Re_c = 200,000$  are presented in Fig. 12 and show quite favorable agreement for the q3D cases.

Drag predictions start to deteriorate at Reynolds numbers of  $Re_c = 300,000$  and above as shown in Fig. 13, showing consistently lower q3D section drag before stall, attributed to the absence of small-scale turbulence in the simulations. For all Reynolds numbers in the experiment, the pressure distributions reveal the presence of separation bubbles. Despite this, the bubble-dominated lift is seen to be predicted

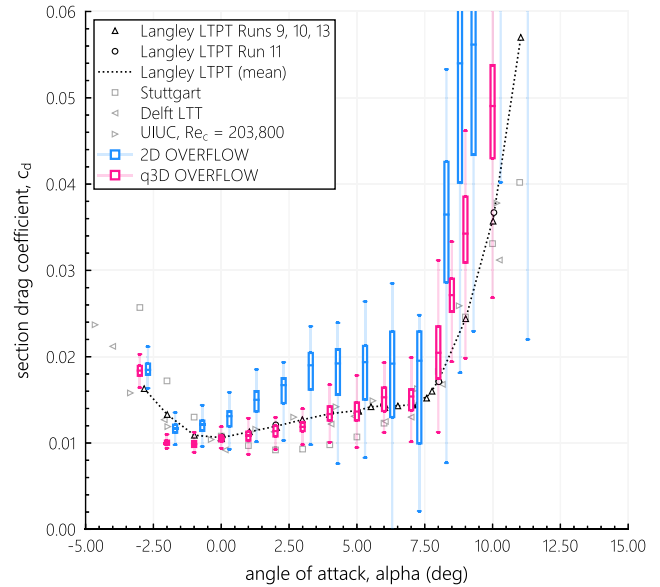


**Fig. 12** Section drag for  $Re_c = 200,000$  compared to available experimental data from Refs. [51–54].

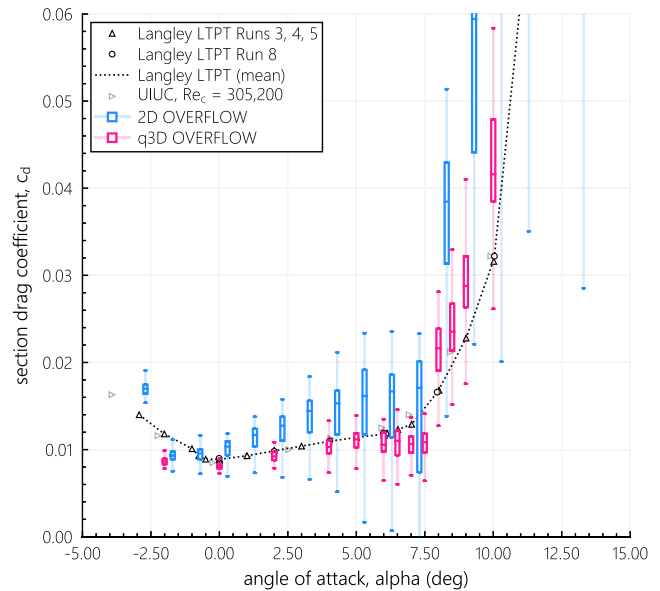


**Fig. 13** Section drag for  $Re_c = 300,000$  compared to available experimental data from Refs. [51,54].

with good accuracy up to the highest Reynolds number in the experiment,  $Re_c = 460,000$ , as presented in Fig. 14.

Therefore, the transition to small-scale turbulence (first occurrences observed in Ref. [51] near stall for  $Re_c = 200,000$  to  $Re_c = 300,000$ ) is unlikely to be the cause of the bubble reattachment but could simply be an unavoidable side effect of the growing shear layer instabilities (the pressure distributions will be shown in the following section). Tables 3 and 4 show mean aerodynamic coefficients for all Reynolds numbers tested at  $\alpha = 2^\circ$ .

Both lift and drag for q3D are predicted within 10% for the q3D cases, except for the highest Reynolds number, where drag starts to be underpredicted. Tables 5 and 6 show time-averaged aerodynamic coefficients for all Reynolds numbers tested at  $\alpha = 4^\circ$ . For  $Re_c = 60,000$  results for both flow states, laminar separation (LS) and turbulent reattachment (TR) are presented. Both LS and TR flow states are presented separately for experimental LTPT results at  $Re_c = 60,000$  in Tables 5–8. Numerical results for  $Re_c = 60,000$ , however, correspond to just one simulation, and the relative error indicates which flow state is predominantly observed.

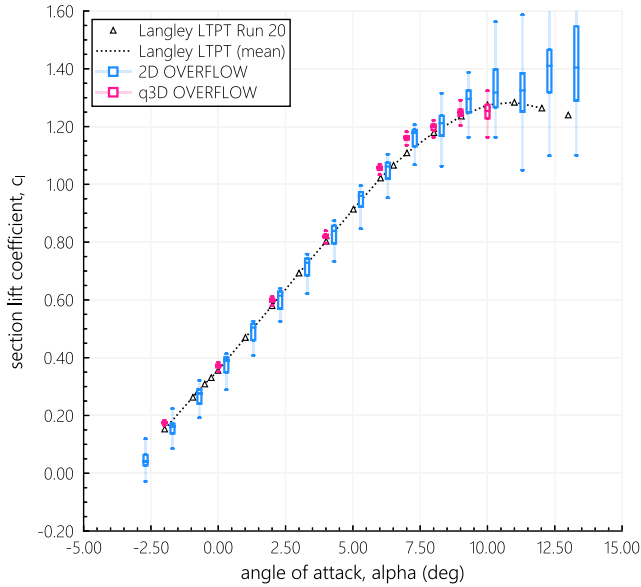


**Fig. 14** Section lift for  $Re_c = 460,000$  compared to available experimental data from Refs. [51].

**Table 3** Mean section lift for  $\alpha = 2^\circ$  compared to LTPT data [51]

Reynolds number, $Re_c$	Section lift coefficient, $c_l$			Relative error, %	
	2D	q3D	LTPT	2D	q3D
60,000	0.687	0.512	0.559	22.9	-8.4
100,000	0.649	0.589	0.586	10.8	0.5
200,000	0.595	0.604	0.574	3.7	5.2
300,000	0.590	0.613	0.572	3.1	7.2
460,000	0.600	0.598	0.580	3.4	3.1

**Table 4** Mean section drag for  $\alpha = 2^\circ$  compared to LTPT data [51]

Reynolds number, $Re_c$	Section drag coefficient, $c_d$			Relative error, %	
	2D	q3D	LTPT	2D	q3D
60,000	0.0318	0.0345	0.0322	-1.2	7.1
100,000	0.0258	0.0216	0.0211	22.3	2.4
200,000	0.0159	0.0113	0.0118	34.7	-5.1
300,000	0.0121	0.0093	0.0099	22.2	-6.1
460,000	0.0078	0.0059	0.0078	0.0	-24.4

**Table 5** Mean section lift for  $\alpha = 4^\circ$  compared to LTPT data [51]

Reynolds number, $Re_c$	Section lift coefficient, $c_l$			Relative error, %	
	2D	q3D	LTPT	2D	q3D
60,000 (LS)	0.851	0.642	0.645	31.9	-0.5
60,000 (TR)	—	—	0.721	18.0	-11.0
100,000	0.820	0.769	0.778	5.4	-1.1
200,000	0.799	0.826	0.785	1.8	5.2
300,000	0.799	0.835	0.792	0.9	5.4
460,000	0.825	0.819	0.803	2.7	2.0

At the higher angles of attack the lift prediction improves for  $Re_c > 60,000$ , with a maximum error in lift prediction for the q3D simulations of 5.4%. The drag coefficient error stays within 8.7% except for the highest Reynolds number. Tables 7 and 8 show mean aerodynamic coefficients for all Reynolds numbers tested at  $\alpha = 6^\circ$ .

**Table 6** Mean section drag for  $\alpha = 4^\circ$  compared to LTPT data [51]

Reynolds number, $Re_c$	Section drag coefficient, $c_d$			Relative error, %	
	2D	q3D	LTPT	2D	q3D
60,000 (LS)	0.0394	0.0408	0.0447	-11.9	-8.7
60,000 (TR)	—	—	0.0400	-1.5	2.0
100,000	0.0298	0.0248	0.0230	29.6	7.8
200,000	0.0181	0.0134	0.0133	36.1	0.8
300,000	0.0142	0.0104	0.0109	30.3	-4.6
460,000	0.0095	0.0067	0.0090	5.6	-25.6

**Table 7** Mean section lift for  $\alpha = 6^\circ$  compared to LTPT data [51]

Reynolds number, $Re_c$	Section lift coefficient, $c_l$			Relative error, %	
	2D	q3D	LTPT	2D	q3D
60,000 (LS)	0.978	0.833	0.661	48.0	26.0
60,000 (TR)	—	—	0.939 <sup>a</sup>	4.2	-11.3
100,000	0.981	0.973	0.974	0.8	-0.1
200,000	0.992	1.031	1.004	-1.2	2.7
300,000	1.049	1.049	1.010	3.9	3.9
460,000	1.046	1.055	1.022	2.3	3.2

<sup>a</sup>Interpolated from neighboring angles of attack.

**Table 8** Mean section drag for  $\alpha = 6^\circ$  compared to LTPT data [51]

Reynolds number, $Re_c$	Section drag coefficient, $c_d$			Relative error, %	
	2D	q3D	LTPT	2D	q3D
60,000 (LS)	0.0402	0.0432	0.0639	-37.1	-32.4
60,000 (TR)	—	—	0.0388 <sup>a</sup>	3.6	11.3
100,000	0.0256	0.0252	0.0224	14.3	12.5
200,000	0.0179	0.0151	0.0141	27.0	7.1
300,000	0.0140	0.0107	0.0116	20.7	7.8
460,000	0.0110	0.0078	0.0101	8.9	-222.8

<sup>a</sup>Interpolated from neighboring angles of attack.

Comparison between simulation and experiment degrades toward higher angles of attack, near stall onset, as the flowfield gets more complex. The results that correlate best with measurements are obtained at  $Re_c = 100,000$  to  $Re_c = 300,000$ ; at lower Reynolds numbers, reattachment fails to occur reliably (the airfoil is on the verge of stalling). At higher Reynolds numbers the drag errors become substantial—presumably due to non-negligible contribution of small-scale turbulence, even though the pressure distributions are still showing accurate capturing of the mean bubble geometry. Table 9 summarizes the average absolute value errors (up to stall) for each Reynolds number group, compared to LTPT data ( $\alpha = -3^\circ$  to  $\alpha < 8^\circ$ ). Cases at  $Re_c = 60,000$  are excluded due to the dual flow state between  $\alpha = 2.5^\circ$  to  $\alpha = 7.5^\circ$ , and due to inconsistent reattachment behavior.

### B. Mean Pressure Distributions

As mean integrated aerodynamic forces can still give a skewed observation of the accuracy of the predicted section lift, the pressure

**Table 9** Quasi-3D errors before stall compared to LTPT data [51]

Reynolds number, $Re_c$	Averaged absolute errors for q3D, %	
	Section lift, $c_l$	Section drag, $c_d$
100,000	3.2	6.6
200,000	6.2	5.1
300,000	6.6	9.6
460,000	5.3	22.9

distributions for representative cases are shown below. The distributions show the influence of the spanwise dependence of the flow on the results clearly, although all 2D simulations are seen to capture the major dynamics (including reattachment region). The good agreement between the q3D pressure distribution and the experimental pressure distribution (both obtained from the centerline of the 3D airfoil) shows that the bubble dynamics in the mean flow are accurately captured.

Cases at  $Re_c = 60,000$  see a pressure peak just too late to provide mean reattached flow. Figure 15 shows the pressure distribution for  $\alpha = 2^\circ$  at  $Re_c = 60,000$ . The 2D cases see an additional reduction in pressure distribution due to a nested secondary bubble.

Toward higher Reynolds numbers the pressure distributions can be seen to agree well for the q3D cases. Figures 16 and 17 show the mean pressure distribution for  $Re_c = 100,000$  and  $Re_c = 200,000$ ,

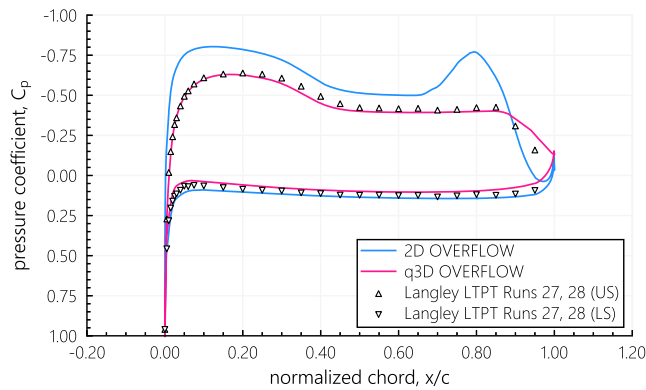


**Fig. 15** Mean pressure distributions for  $\alpha = 2^\circ$  and  $Re_c = 60,000$  compared to LTPT data [51].

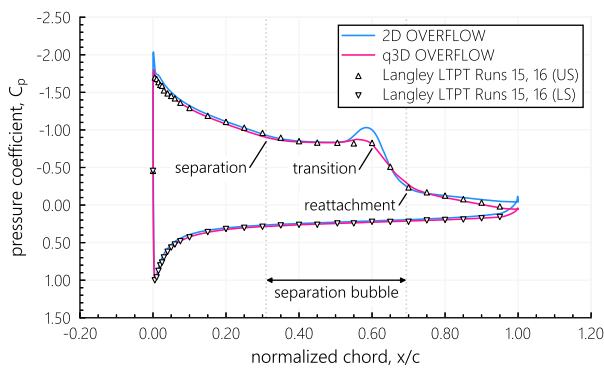


**Fig. 16** Mean pressure distributions for  $\alpha = 6^\circ$  and  $Re_c = 100,000$  compared to LTPT data [51].

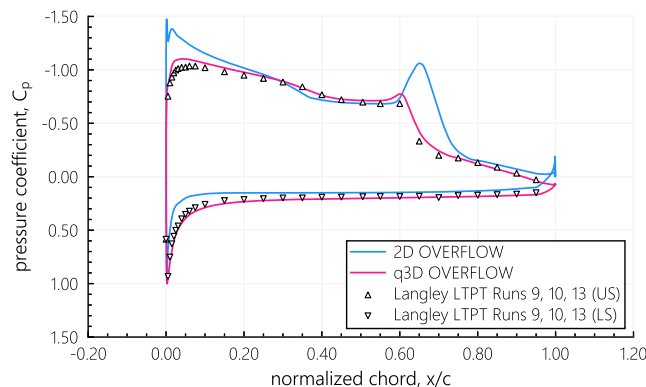


**Fig. 17** Mean pressure distributions for  $\alpha = 4^\circ$  and  $Re_c = 200,000$  compared to LTPT data [51].

respectively. The figures show good agreement of the pressure distribution using the q3D simulations.

The plateau and pressure rise in the mean pressure distribution are indicative of the bubble separation, transition, and reattachment [10,34], as illustrated in Fig. 16. At  $Re_c = 300,000$  the bubble length diminishes and is also less accurately captured (see Fig. 18).

Toward higher angles of attack near stall, a bubble is predicted in the simulations, but not observed from the experimental pressure distributions. At  $Re_c = 300,000$  and  $\alpha = 8^\circ$  the LTPT data indicate natural transition (NT) at  $x/c = 0.20$ . The simulations are unable to capture the natural transition, but still accurately obtain the pressure distribution over the aft section of the airfoil, as shown in Fig. 19.

The pressure distributions still provide good correlation with the experimental data before stall, even at  $Re_c = 460,000$ , as shown in Fig. 20.

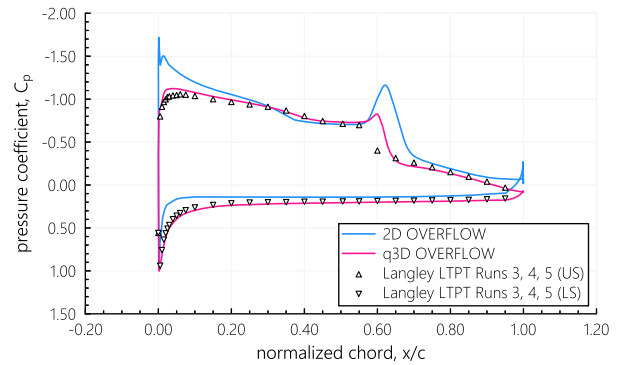


**Fig. 18** Mean pressure distributions for  $\alpha = 4^\circ$  and  $Re_c = 300,000$  compared to LTPT data [51].

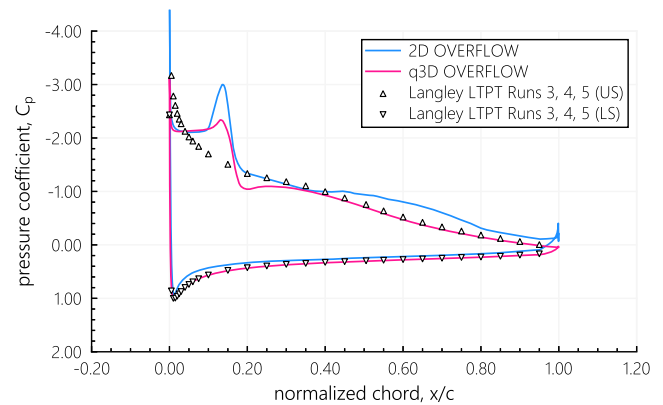


**Fig. 19** Mean pressure distributions for  $\alpha = 8^\circ$  and  $Re_c = 300,000$  compared to LTPT data [51].

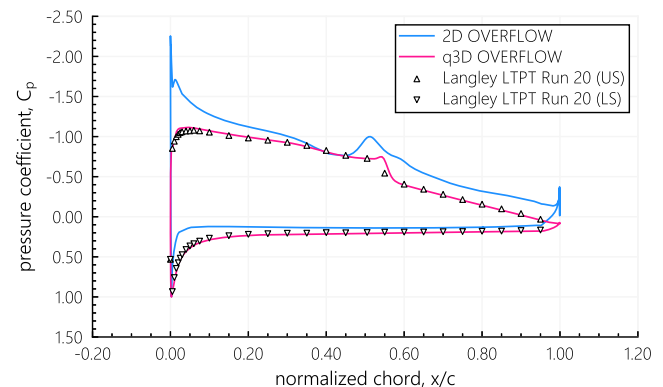


**Fig. 20** Mean pressure distributions for  $\alpha = 4^\circ$  and  $Re_c = 460,000$  compared to LTPT data [51].

### C. Separation–Reattachment Locations

The experimental data included separation and reattachment locations using oil-film techniques for  $Re_c = 100,000$  to  $Re_c = 300,000$  [51]. At lower Reynolds numbers, the mean flow barely reattaches and is essentially stalled, prohibiting consistent observation of the separation and reattachment locations.

The skin friction from the simulation is used to map the laminar separation and turbulent reattachment of the flow. The locations are only computed for the upper surface from the stagnation point up to the TE. The first occurrence downstream from the stagnation point where the mean skin friction reaches  $C_f = 0$  is identified as the laminar separation (LS) location. The following downstream location within the overall bubble shape where a mean positive skin friction is obtained is identified as the turbulent reattachment location (TR), as done in Ref. [55]. Figure 21 shows the experimental separation–reattachment locations and both 2D and q3D simulation results for  $Re_c = 100,000$ . The OVERFLOW simulations are referred to as “2D” and “q3D.” The onset of stall is estimated by marking the first (experimental) angle of attack where  $\delta(c_1/c_d)/\delta\alpha < 0$  occurs.

Most of the simulations show the existence of a nested secondary bubble within the primary separation region where, because of the reversed flow in the primary bubble, there is a reattachment upstream of the primary turbulent reattachment. No mention of a secondary separation bubble was made in the experiments [51,55] and the separation–reattachment locations of the nested bubble have not been plotted in Figs. 21, 22, and 24 for clarity of the figures.

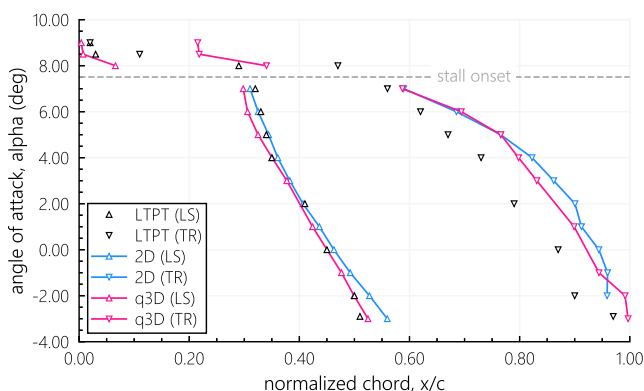


**Fig. 21** Laminar separation and mean turbulent reattachment locations for  $Re_c = 100,000$  compared to LTPPT data [51].

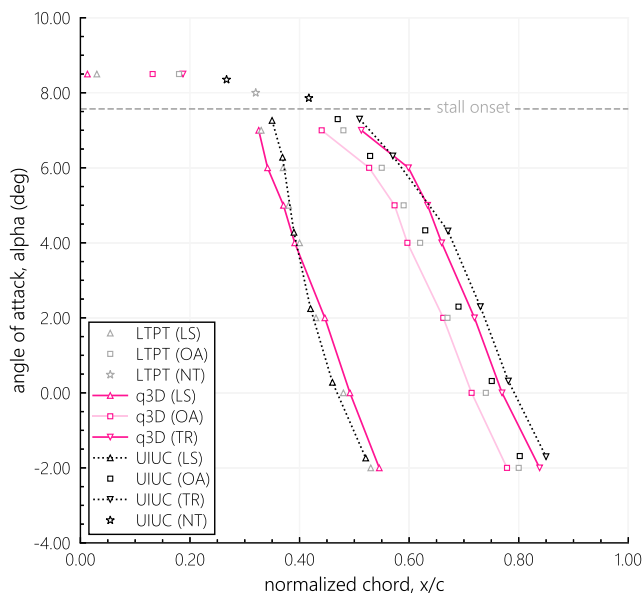


**Fig. 22** Laminar separation and mean turbulent reattachment locations for  $Re_c = 200,000$  compared to experimental data from Refs. [51,55].

For all simulations, LS and TR are only observed in the time-averaged sense; there is no bubble in the time-accurate sense (only large-scale unsteady structures are observed, characteristic of *bubble flapping*). Some values (stall and beyond) provide large sets of skin friction sign switches in the mean flow and are omitted (no time-averaged bubble is observed, just separated flow).

For  $Re_c = 100,000$  the reattachment location is seen to be roughly at a constant offset from the experimental values, and for the q3D cases, the average error in reattachment location prediction before stall is around  $0.07c$ . The pressure distributions in the previous section seem to indicate higher mean reattachment location accuracy, because the distinct pressure increase is predicted well (see Fig. 16), which is often correlated to the reattachment location [22,40].

In Ref. [55] it is shown that there exists a small gap between oil accumulation and actual flow reattachment in experimental studies. From this it is hypothesized that the oil-accumulation line was misinterpreted in Ref. [51] as the reattachment line. Testing in Ref. [55] was performed for the Eppler 387 airfoil at  $Re_c = 200,000$  and  $Re_c = 300,000$  and the LS, oil accumulation (OA), and TR locations were recorded. Runs at  $Re_c = 100,000$  were omitted because they required excessive runtime to establish the oil pattern. Figure 22 shows the comparison of the simulations with the added experimental data from Ref. [55] for  $Re_c = 200,000$  marked “UIUC,” showing greatly improved agreement. Note that the LTPT turbulent reattachment locations have now been labeled as oil accumulation (OA) locations.

The time-averaged skin friction for  $Re_c = 200,000$  and  $\alpha = 4^\circ$  is plotted in Fig. 23 and shows favorable agreement to the conceptual skin friction distribution in Ref. [55]. The figure also presents the secondary separation bubble (within the primary separation bubble, with reattachment upstream of the primary turbulent reattachment). Arrows indicate the direction of the wall shear stress for clarity.

Comparison to UIUC data is favorable for  $Re_c = 200,000$  and  $\alpha = 4^\circ$  and shows average errors of  $0.01c$ ,  $0.04c$ , and  $0.02c$  for the LS, OA, and TR locations, respectively. The data for  $Re_c = 300,000$  are plotted in Fig. 24. On average 3D laminar separation location errors are around  $1\%c$  and reattachment locations show a  $3\%c$  error.

The progressively increasing error in reattachment location prediction with angle of attack (see also the pressure distribution in Fig. 18) is likely the onset of the influence of small-scale turbulence, promoting earlier mean reattachment upstream.

When the simulation results are compared to the experimental UIUC data for  $Re_c = 200,000$  and  $Re_c = 300,000$  (linearly interpolated to the simulation angles of attack), the absolute average value errors for turbulent reattachment before stall are improved, as summarized in Table 10. For  $Re_c = 200,000$  the laminar separation location errors before stall range between  $-3.3\%c$  and  $-0.2\%c$  for 2D and  $-3.0\%c$  and  $2.9\%c$  for q3D. The corresponding turbulent reattachment location errors range from  $-5.3\%c$  to  $6.0\%c$  for 2D and  $1.3\%c$  to  $2.2\%c$  for q3D. For  $Re_c = 300,000$  the laminar separation location errors before stall range between  $-3.6\%c$  and  $-1.5\%c$  for 2D and  $-1.9\%c$  and  $1.3\%c$  for q3D. The corresponding turbulent

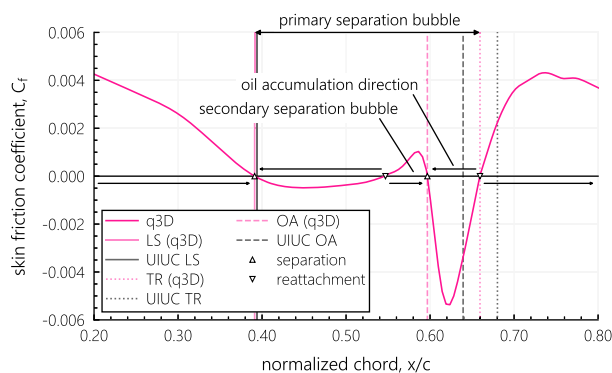


**Fig. 23** Skin friction coefficient versus chord for  $Re_c = 200,000$  and  $\alpha = 4^\circ$  compared to UIUC data [55].

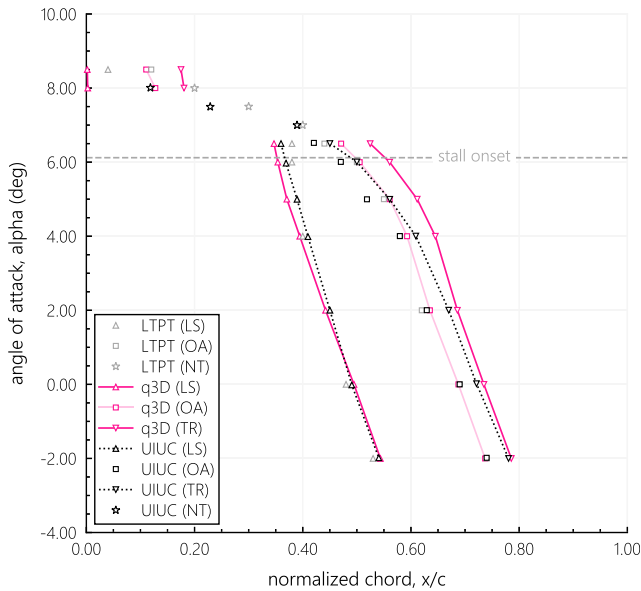


**Fig. 24** Laminar separation and mean turbulent reattachment locations for  $Re_c = 300,000$  compared to experimental data from Refs. [51,55].

**Table 10** Separation–reattachment errors compared to UIUC data [55]

Case		Averaged absolute error, %c	
		$Re_c = 200,000$	$Re_c = 300,000$
LS	2D	1.6	2.6
	q3D	2.1	1.2
TR	2D	4.0	6.2
	q3D	1.9	3.0

reattachment location errors range from 4.7%*c* to 7.2%*c* for 2D and 0.5%*c* to 6.0%*c* for q3D.

## V. Discussion

This section discusses differences between the 2D and q3D simulations, the modeling of bubble flapping, a proposed explanation for the oil accumulation, and a preliminary analysis on the dual-flow state observed at  $Re_c = 60,000$ .

### A. Importance of Spanwise Flow: 2D-q3D Differences

Simulations using 2D unsteady NS are often considered inappropriate for bluff body aerodynamics because the influence of the spanwise component is crucial [64,72]. The differences between 2D and q3D simulations in the present work can occur largely for two reasons: the introduction of end-effects from the spanwise boundary conditions in q3D simulations, and changes in flow behavior due to the presence of the spanwise coordinate. Both are observed in the present work.

In the pressure distributions in Figs. 15–20, the higher suction peak for the 2D simulations alludes to the strictly 2D performance of the airfoil, practically always resulting in higher section lift than its q3D counterpart. The vortical structures in 2D have no means to diffuse into 3D structures, resulting in prolonged vortex convection compared to q3D cases. The differences in vortex convection length are clearly shown for the case of  $\alpha = 8.5^\circ$  and  $Re_c = 100,000$  by plotting an isosurface of the  $Q$ -criterion colored by velocity magnitude for both 2D and q3D simulations, as shown in Figs. 25 and 26, respectively.

The q3D case shows a clear view of the spanwise vortices and the downstream instabilities that start to perturb the spanwise structure, resulting in a cascade into smaller structures. Despite these obvious differences, the mean behavior of the airfoils shows very similar

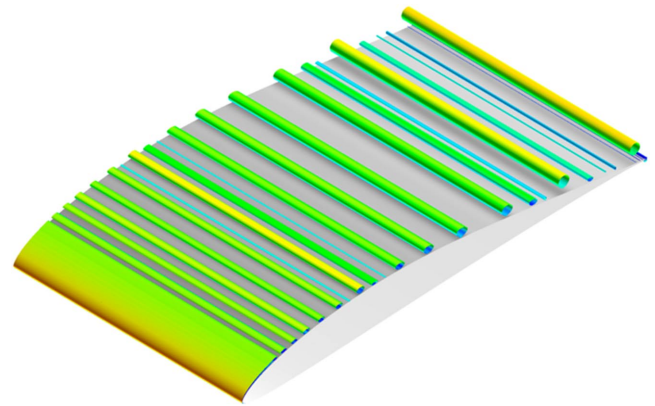


**Fig. 25** Two-dimensional,  $Re_c = 100,000$ , isosurface of  $Q$ -criterion colored by velocity magnitude,  $\alpha = 8.5^\circ$ .

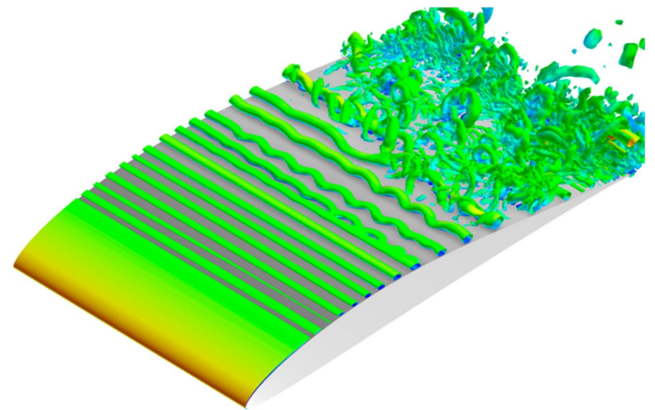


**Fig. 26** Quasi-3D,  $Re_c = 100,000$ , isosurface of  $Q$ -criterion colored by velocity magnitude,  $\alpha = 8.5^\circ$ .

separation–reattachment locations and pressure distributions (see Figs. 15–20). Comparison of integrated aerodynamic coefficients with tunnel results, however, was only favorable for the q3D cases, showing a clear influence of the end-effects and spanwise dimension, in comparison to the 2D cases.

Lin and Pauley [23] present 2D laminar UNS analyses for the same airfoil and compared to a selection of cases from the same LTPT experimental data, showing good pressure distribution and separation–reattachment agreement with the LTPT data, and comparable errors in lift and drag estimation to the q3D results in the present work. It is unclear to the authors what the cause is of this good agreement, as the criticality of the end-effects and spanwise dimension on reverse velocities in the bubble are shown to be influential in the present work.

### B. Modeling of Flapping Laminar Separation Bubbles

Analyses of LSBs are challenging due to their inherent complexity and the susceptibility to various flow disturbances through receptivity influences for laminar near-wall flows [25,30]. Furthermore, the characteristics of the vortices formed in the separation bubble are dependent on the pressure distribution, resulting in a dependence on airfoil geometry, Reynolds number, and angle of attack [23].

The good pressure distribution correlation supports the hypothesis that bubble behavior here is not governed by small-scale turbulence (as this cannot be modeled in the unsteady laminar NS simulations), but rather by large vortical structures that dominate performance and only in a time-averaged sense resemble a reattached boundary layer. It is key to note that reattachment for all cases is only observed in the mean flow. Even at the highest Reynolds number tested of  $Re_c = 460,000$  the pressure distribution still shows good predictions of bubble-dominated lift before stall (see Fig. 20), implying that the bubble flapping behavior can be governed by large scales up to

relatively high Reynolds numbers, usually thought to be the realm of “steady reattachment” bubbles.

Wang et al. [34] investigated the NACA 0012 airfoil at a wide Reynolds number range with varying turbulence intensity of the oncoming flow. The analysis describes eight distinct flow structures in four proposed Reynolds number regimes, as shown in Fig. 27. The switch from bubble flapping (mode D) to steady reattachment (mode E) for changes in angle of attack and Reynolds number for a NACA 0012 airfoil is shown in Fig. 27.

The modeling of bubbles is therefore likely possible until small-scale transition is the cause of separated shear layer reattachment, which then sets the Reynolds number at which relatively steady “ordinary” LSBs start to form. The primary catalysts for steady LSBs to occur are then higher Reynolds numbers, higher freestream turbulence, and higher angles of attack.

The results show that laminar UNS can predict unsteady LSBs (bubble flapping) and also show that the phenomenon can exist without the need for acoustic feedback mechanisms (as discussed in Refs. [25,65]), or interaction with freestream turbulence intensities (as discussed in Ref. [66]). The 2D simulations, unaffected by end effects, show performance differences with q3D simulations as expected, but the separation–reattachment behavior is surprisingly similar, making bubble flapping also possible in 2D and not intrinsically an instability of shed vortices to 3D disturbances (as discussed in Ref. [24]).

A likely candidate for the shear layer instability is the KH instability. The shear layer velocity profile can be decomposed into a constant and equal velocity across the shear layer and a velocity shear component. The velocity shear component results in pressure differences that start the K-H instability and ultimately cause vortex formation, as sketched in Fig. 28. The instability and vortex roll-up is confirmed to be essentially 2D by experiments [39]. The mechanism and flow physics causing bubble flapping are still the subject of ongoing research.

Even when the mean flow reattachment can be accurately predicted using laminar NS, drag is more difficult to predict, most likely due to the omnipresent small-scale turbulence within the boundary layer. For the present Reynolds number range and airfoil, small-scale turbulence is likely a consequence of the breakdown of these turbulent structures,

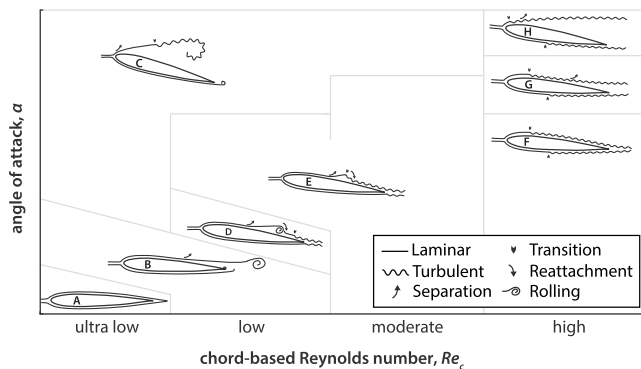


Fig. 27 Schematic of flow structures around NACA 0012 airfoil, from Ref. [34].

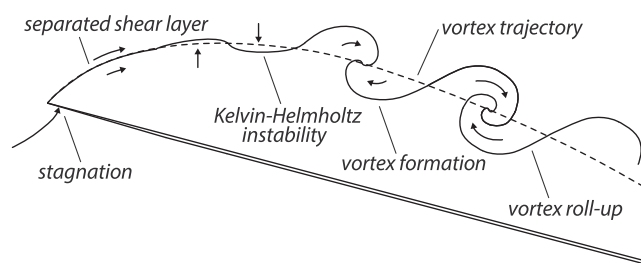


Fig. 28 Schematic representation of vortex roll-up due to the Kelvin-Helmholtz instability of a separated shear layer, from Ref. [73].

rather than the causal mechanism for flow reattachment; this was deduced from the good prediction of the pressure distributions.

The influence of small-scale turbulence is expected to have a more profound impact on drag with increasing Reynolds number, which is observed by the increasingly larger errors in drag predictions toward higher Reynolds numbers above  $Re_c = 300,000$  to  $460,000$  (see Fig. 13) and increase in angle of attack, as also shown experimentally in Ref. [34].

From this it could be concluded that airfoil design for very low Reynolds numbers could be performed using unsteady laminar NS, at least in the early design phase, to reduce computational expense and complexity, compared to inclusion of turbulence and/or transition models in URANS approaches or higher-order methods. The primary reason for this is that the large-scale dynamics can still be captured by a UNS approach to a sufficient degree for the mean aerodynamic performance of the airfoil. Analogously, Hunt [49] states that “quite a few flow regions that appear complex and/or 3D are shaped by ‘vortical inviscid’ physics, and not by the local turbulent stresses,” in line with the hypothesis brought forth in the present work.

The experiments are conducted at relatively low values of FSTI, implying that at higher levels of FSTI the small-scale turbulence is likely to manifest itself more prominently. All experimental data, however, are obtained from different Mach numbers (with different correlated FSTI values), showing no fundamental changes in bubble behavior, suggesting that all FSTI values are below a threshold where small-scale turbulence is dominant for the bubble behavior. At higher Reynolds numbers (or higher levels of FSTI), and/or higher angles of attack, it is expected that the separated shear layer can transition to small-scale turbulence, which consequently induces reattachment. To be able to observe an instantaneous bubble structure, this transition will have to happen before the vortex shedding can occur.

C. Origin of the Oil Accumulation in the Flow Visualization

Selig et al. [55] present a photograph of the experimental flow visualization using oil techniques for the Eppler 387 airfoil at  $Re_c = 5^\circ$  and  $\alpha = 5^\circ$ . Plotting the skin friction and photograph at the same chord scale, the favorable agreement can be seen in Fig. 29.

For the q3D simulations the laminar separation and oil-accumulation line are predicted near 1%*c* of the experimental value, and the turbulent reattachment region within 2%*c*. Considering that the accuracy of experimentally obtaining the data is around 1%*c* to 2%*c* [55], and the maximum chordwise separation for the simulations is 0.5%*c*, the present accuracy is what could be expected at best. Selig et al. [55] state: “[T]he laminar flow smoothly streaks the oil, until ... laminar separation starts. Beyond this point and inside the bubble, there is very little flow and the oil does not change; it keeps

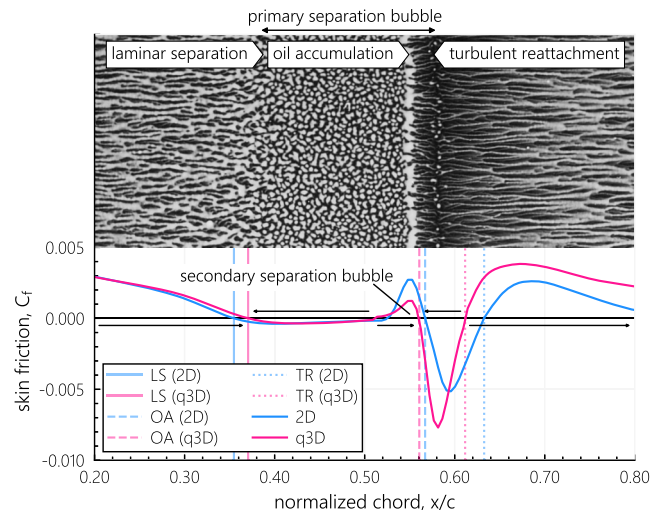


Fig. 29 Skin friction coefficient versus chord for  $Re_c = 300,000$  and  $\alpha = 5^\circ$  compared to UIUC flow visualization [55] (adapted with permission).

the orange-peel textured look. At reattachment . . . the flow impinges on the surface and creates high shear stress that scours away the oil. It moves some oil upstream and some oil downstream as the downflow ‘splashes’ onto the surface effectively creating a ‘continental divide’ defined by a very fine dividing line. The oil moving upstream pools into what we call the ‘oil accumulation line,’ while the oil going downstream moves toward the trailing edge” [55]. As the oil accumulation from the reattachment region *and* the primary surface flow inside the bubble are both upstream, it is not immediately clear why the oil would be accumulated onto a distinct line, or why the skin friction changes so drastically within the bubble. The skin-friction distribution in Fig. 29 shows the existence of a secondary bubble, creating downstream-oriented flow opposing the oil accumulation from the reattachment region, creating an opposing flow of oil and hence an oil accumulation line at the location of flow separation of the nested secondary bubble. The nested bubble therefore provides a reason for the sharp oil accumulation line due to the opposing wall shear stresses and rapid reduction of the skin friction gradient. The secondary bubble velocity and skin friction magnitudes are likely too low to be picked up in the oil flow, and hence not distinctly visible in the “orange peel texture.”

The flow visualization for the q3D case is shown in Fig. 30 as velocity magnitude with overlaid velocity streamlines, showing the primary separation bubble with the nested smaller bubble. The visualization is cropped between  $0.20 < x/c < 0.80$ , for comparison with Fig. 29.

#### D. Dual Flow State at $Re_c = 60,000$

McGhee and Walker [51] state that dual flow states were observed between  $\alpha = 2.5^\circ$  and  $\alpha = 7^\circ$  at  $Re_c = 60,000$ . Moreover, no hysteresis effects were seen, and the effect is observed for all runs (with varying Mach numbers and corresponding freestream conditions). The case for  $\alpha = 6^\circ$  is run for an extended time of  $t = 60$  flow passes. The section drag, including the approximate dual flow state results observed in the LTPT, is shown in Fig. 31.

The corresponding chordwise location of laminar separation is extracted and presented in Fig. 32. The maximum observed variation exceeds  $0.10c$ , but due to the flapping nature of the bubble, (possible) corresponding reattachment locations cannot be readily deduced without selectively choosing averaging windows.

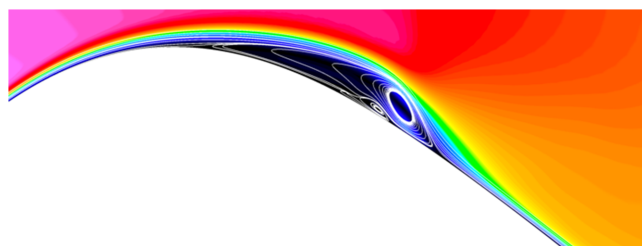


**Fig. 30** Quasi-3D flow visualization of upper surface with streamlines for  $Re_c = 300,000$  and  $\alpha = 5^\circ$  (vertical axis scaled by 5).

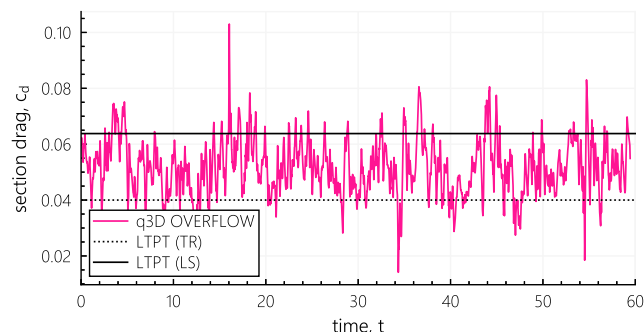


**Fig. 31** Section drag over time for  $\alpha = 6^\circ$  at  $Re_c = 60,000$ .

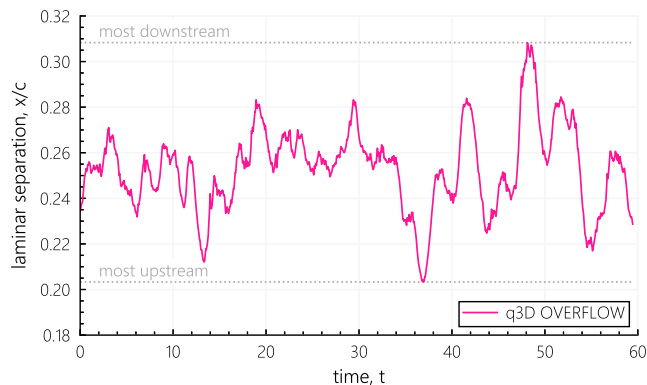


**Fig. 32** Laminar separation location versus time for  $\alpha = 6^\circ$  at  $Re_c = 60,000$ .

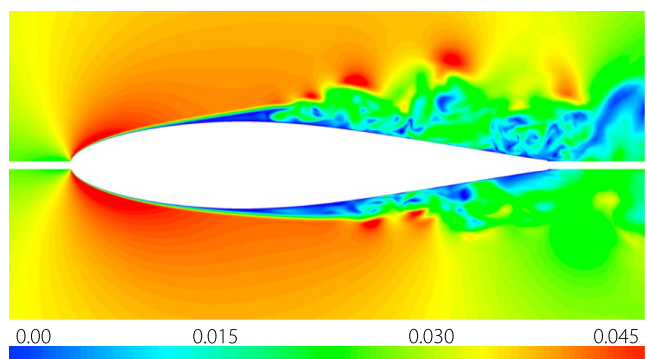


**Fig. 33** Mirrored image of q3D time-accurate Mach number on upper surface at laminar separation (top) and turbulent reattachment (bottom),  $\alpha = 6^\circ$  at  $Re_c = 60,000$ .

Figure 33 shows the Mach number over the upper surface of the Eppler 387 airfoil for the most upstream laminar separation location (top) and the most downstream laminar separation location (bottom).

As no upstream disturbances are introduced, the behavior is self-sustained and could be induced by the reversed flow inside the bubble. The behavior might be a phenomenon occurring just because the airfoil is on the verge of stalling and barely reattaches in most conditions. Momentary unsteady reattachment could largely affect the flow and mean behavior of the airfoil, making it particularly sensitive to operating conditions.

## VI. Conclusions

Lift on the Eppler 387 airfoil is bubble dominated at around  $Re_c = 460,000$  and below. The LSBs do not feature steady reattachment, but large-scale spanwise structures are found to shed into the turbulent boundary layer, which is only reattached in a time-averaged sense. This is referred to as bubble flapping. Laminar unsteady NS simulations in 3D and 2D are compared to experimental work for  $Re_c = 60,000$  to  $Re_c = 460,000$ .

The primary differences between 2D and q3D cases were substantially lower suction peaks for q3D cases, and a stronger recirculation in the bubble for 2D cases (locally slightly increasing lift). Average absolute value lift and drag predictions for  $Re_c = 100,000$  to  $300,000$  differ by 5 to 7% compared to experimental data, respectively. Below  $Re_c = 60,000$  no reliable time-averaged reattachment was observed, leaving the airfoil essentially stalled. Drag predictions at  $Re_c = 460,000$  are off considerably, likely due to the small-scale turbulence that begins to have a dominant impact on drag and bubble behavior. Despite this, lift predictions are still good at  $Re_c = 460,000$  with good mean pressure distribution comparisons for all but the highest angles of attack, indicating that the bubble flapping is still the dominant instability in the flow.

Good agreement of the mean pressure distributions is obtained for nearly all cases, including the characteristic “plateau” in the LSB, and

the adverse pressure gradient indicative of transition and subsequent mean-flow reattachment. Laminar unsteady NS without turbulence and/or transition models is capable of resolving the bubble dynamics, with laminar separation predictions on average within around 2% (close to the estimated experimental accuracy of around 1% to 2%), and turbulent reattachment around 5% for  $Re_c = 100,000$  to  $300,000$ , compared to LTPT experimental results before stall. Comparing with the suggested corrections by UIUC due to a hypothesized mis-observed reattachment region, turbulent reattachment on average improves to 3% for  $Re_c = 200,000$  to  $300,000$ , before stall. A nested secondary bubble (within the primary separation bubble) is presented as the reason for the experimentally observed oil-accumulation line.

The work shows that bubble flapping predictions can be made using laminar UNS, and that their existence does not necessitate external influences such as acoustic sources or freestream turbulence. Even in strictly 2D simulations the global bubble flapping separation, transition, and reattachment trends are similar. This is in general agreement with the findings determining that, at low enough level of external influence, the shear layer transition will be dominated by 2D vortex shedding and that small-scale oscillations and the large-scale vortex shedding are independent.

### Acknowledgments

The research of Witold J. F. Koning, Haley Cummings, and Brenda Natalia Perez Perez is made possible by the NASA FY21 Space Technology Mission Directorate Early Career Initiative Project “Rotor Optimization for the Advancement of Mars eXploration.” Pieter Buning and Ethan Romander were supported by the NASA Revolutionary Vertical Lift Technology Project. The authors would like to acknowledge the support of William Warmbrodt and Larry Hogle during this research. Thomas Pulliam and Wayne Johnson are thanked for their feedback in reviewing this paper. Resources supporting this work were provided by the NASA High-End Computing Program through the NASA Advanced Supercomputing Division at Ames Research Center.

### References

- [1] Carmichael, B. H., “Low Reynolds Number Airfoil Survey, Volume 1,” NASA CR-165803-VOL-1, 1981.
- [2] Lissaman, P. B. S., “Low-Reynolds-Number Airfoils,” *Annual Review of Fluid Mechanics*, Vol. 15, No. 1, 1983, pp. 223–239. <https://doi.org/10.1146/annurev.fl.15.010183.001255>
- [3] Mueller, T. J., and DeLaurier, J. D., “Aerodynamics of Small Vehicles,” *Annual Review of Fluid Mechanics*, Vol. 35, Jan. 2003, pp. 89–111. <https://doi.org/10.1146/annurev.fluid.35.101101.161102>
- [4] Pines, D. J., and Bohorquez, F., “Challenges Facing Future Micro-Air-Vehicle Development,” *Journal of Aircraft*, Vol. 43, No. 2, March 2006, pp. 290–305. <https://doi.org/10.2514/1.4922>
- [5] Hoerner, S. F., *Fluid-Dynamic Drag: Practical Information on Aerodynamic Drag and Hydrodynamic Resistance*, Hoerner Fluid Dynamics, Bricktown, NJ, 1965, Chaps. 3, 5, 6, 15, 19.
- [6] Winslow, J., Otsuka, H., Govindarajan, B., and Chopra, I., “Basic Understanding of Airfoil Characteristics at Low Reynolds Numbers (104–105),” *Journal of Aircraft*, Vol. 55, No. 3, May 2018, pp. 1050–1061. <https://doi.org/10.2514/1.C034415>
- [7] Lee, D., Nonomura, T., Oyama, A., and Fujii, K., “Comparative Studies of Numerical Methods for Evaluating Aerodynamic Characteristics of Two-Dimensional Airfoil at Low Reynolds Numbers,” *International Journal of Computational Fluid Dynamics*, Vol. 31, No. 1, 2017, pp. 57–67. <https://doi.org/10.1080/10618562.2016.1274398>
- [8] Lee, D., Kawai, S., Nonomura, T., Anyoji, M., Aono, H., Oyama, A., Asai, K., and Fujii, K., “Mechanisms of Surface Pressure Distribution Within a Laminar Separation Bubble at Different Reynolds Numbers,” *Physics of Fluids*, Vol. 27, No. 2, 2015, Paper 023602. <https://doi.org/10.1063/1.4913500>
- [9] Kojima, R., Nonomura, T., Oyama, A., and Fujii, K., “Large-Eddy Simulation of Low-Reynolds-Number Flow over Thick and Thin NACA Airfoils,” *Journal of Aircraft*, Vol. 50, No. 1, 2013, pp. 187–196. <https://doi.org/10.2514/1.C031849>
- [10] O’Meara, M., and Mueller, T. J., “Laminar Separation Bubble Characteristics on an Airfoil at Low Reynolds Numbers,” *AIAA Journal*, Vol. 25, No. 8, Aug. 1987, pp. 1033–1041. <https://doi.org/10.2514/3.9739>
- [11] Schlichting, H., and Kestin, J., *Boundary-Layer Theory*, 7th ed., McGraw-Hill, New York, 1979, Chaps. 2, 7, 10, 13, 16, 17.
- [12] Drela, M., *Flight Vehicle Aerodynamics*, The MIT Press, London, Feb. 2014, Chaps. 1, 4.
- [13] Fitzgerald, E. J., and Mueller, T. J., “Measurements in a Separation Bubble on an Airfoil Using Laser Velocimetry,” *AIAA Journal*, Vol. 28, No. 4, April 1990, pp. 584–592. <https://doi.org/10.2514/3.10433>
- [14] Schmitz, F. W., “Aerodynamics of the Model Airplane. Part 1—Airfoil Measurements,” NASA TM-X-60976, 1967.
- [15] Hoerner, S. F., and Borst, H. V., *Fluid-Dynamic Lift: Practical Information on Aerodynamic and Hydrodynamic Lift*, Hoerner Fluid Dynamics, Bricktown, NJ, 1985, Chaps. 3, 5, 6, 15, 19.
- [16] McMasters, J., and Henderson, M., “Low-Speed Single-Element Airfoil Synthesis,” *Technical Soaring*, Vol. 6, No. 2, 1980, pp. 1–21.
- [17] Saric, W. S., Reed, H. L., and Kerschen, E. J., “Boundary-Layer Receptivity to Freestream Disturbances,” *Annual Review of Fluid Mechanics*, Vol. 34, No. 1, Jan. 2002, pp. 291–319. <https://doi.org/10.1146/annurev.fluid.34.082701.161921>
- [18] Balzer, W., and Fasel, H., “Direct Numerical Simulation of Laminar Boundary-Layer Separation and Separation Control on the Suction Side of an Airfoil at Low Reynolds Number Conditions,” *40th Fluid Dynamics Conference and Exhibit*, AIAA Paper 2010-4866, June–July 2010. <https://doi.org/10.2514/6.2010-4866>
- [19] Boiko, A. V., Grek, G. R., Dovgal, A. V., and Kozlov, V. V., *The Origin of Turbulence in Near-Wall Flows*, Springer Science & Business Media, New York, 2022, Chaps. 2, 3, 4, 6. [https://www.google.com/books/newton/The\\_Origin\\_of\\_Turbulence\\_in\\_Near-Wall\\_Fl/Aij7CAAQB\\_AJ?hl=en&gbpv=1&printsec=frontcover](https://www.google.com/books/newton/The_Origin_of_Turbulence_in_Near-Wall_Fl/Aij7CAAQB_AJ?hl=en&gbpv=1&printsec=frontcover). <https://doi.org/10.1007/978-3-662-04765-1>
- [20] Fisher, A., “The Effect of Freestream Turbulence on Fixed and Flapping Micro Air Vehicle Wings,” Thesis, School of Aerospace, Mechanical and Manufacturing Engineering, RMIT Univ., Melbourne, Australia, June 2013.
- [21] Pauley, L. L., Moin, P., and Reynolds, W. C., “The Structure of Two-Dimensional Separation,” *Journal of Fluid Mechanics*, Vol. 220, Nov. 1990, pp. 397–411. <https://doi.org/10.1017/S0022112090003317>
- [22] Watmuff, J. H., “Evolution of a Wave Packet into Vortex Loops in a Laminar Separation Bubble,” *Journal of Fluid Mechanics*, Vol. 397, Oct. 1999, pp. 119–169. <https://doi.org/10.1017/S0022112099006138>
- [23] Lin, J. C. M., and Pauley, L. L., “Low-Reynolds-Number Separation on an Airfoil,” *AIAA Journal*, Vol. 34, No. 8, Aug. 1996, pp. 1570–1577. <https://doi.org/10.2514/3.13273>
- [24] Abdalla, I. E., and Yang, Z., “Numerical Study of the Instability Mechanism in Transitional Separating-Reattaching Flow,” *International Journal of Heat and Fluid Flow*, Vol. 25, No. 4, 2004, pp. 593–605. <https://doi.org/10.1016/j.ijheatfluidflow.2004.01.004>
- [25] Yarusevych, S., Sullivan, P. E., and Kawall, J. G., “Coherent Structures in an Airfoil Boundary Layer and Wake at Low Reynolds Numbers,” *Physics of Fluids*, Vol. 18, No. 4, 2006, Paper 44101. <https://doi.org/10.1063/1.2187069>
- [26] Windte, J., Scholz, U., and Radespiel, R., “Validation of the RANS-Simulation of Laminar Separation Bubbles on Airfoils,” *Aerospace Science and Technology*, Vol. 10, No. 6, March 2006, pp. 484–494. <https://doi.org/10.1016/j.ast.2006.03.008>
- [27] Rist, U., and Maucher, U., “Investigations of Time-Growing Instabilities in Laminar Separation Bubbles,” *European Journal of Mechanics-B/Fluids*, Vol. 21, No. 5, Oct. 2002, pp. 495–509. [https://doi.org/10.1016/S0997-7546\(02\)01205-0](https://doi.org/10.1016/S0997-7546(02)01205-0)
- [28] Jones, L. E., Sandberg, R. D., and Sandham, N. D., “Direct Numerical Simulations of Forced and Unforced Separation Bubbles on an Airfoil at Incidence,” *Journal of Fluid Mechanics*, Vol. 602, May 2008, pp. 175–207. <https://doi.org/10.1017/S0022112008000864>
- [29] Jones, L. E., Sandberg, R. D., and Sandham, N. D., “Stability and Receptivity Characteristics of a Laminar Separation Bubble on an Aerofoil,” *Journal of Fluid Mechanics*, Vol. 648, April 2010, pp. 257–296. <https://doi.org/10.1017/S0022112009993089>
- [30] Boiko, A. V., Dovgal, A. V., Grek, G. R., and Kozlov, V. V., *Physics of Transitional Shear Flows: Instability and Laminar-Turbulent Transition in Incompressible Near-Wall Shear Layers*, Springer Science &

- Business Media, London, New York, 2011, Chaps. 6, 7, [https://www.google.com/books/edition/Physics\\_of\\_Transitional\\_Shear\\_Flows/zq80hfc9xnQC?hl=en&gbpv=1&printsec=frontcover](https://www.google.com/books/edition/Physics_of_Transitional_Shear_Flows/zq80hfc9xnQC?hl=en&gbpv=1&printsec=frontcover).
- [31] Brendel, M., and Mueller, T. J., "Boundary-Layer Measurements on an Airfoil at Low Reynolds Numbers," *Journal of Aircraft*, Vol. 25, No. 7, July 1988, pp. 612–617. <https://doi.org/10.2514/3.45631>
- [32] Boutillier, M. S. H., and Yarusevych, S., "Separated Shear Layer Transition over an Airfoil at a Low Reynolds Number," *Physics of Fluids*, Vol. 24, No. 8, July 2012, Paper 84105. <https://doi.org/10.1063/1.4744989>
- [33] Gaster, M., "The Structure and Behaviour of Laminar Separation Bubbles," HM Stationery Office R. & M. No. 3595, 1969.
- [34] Wang, S., Zhou, Y., Alam, M. M., and Yang, H., "Turbulent Intensity and Reynolds Number Effects on an Airfoil at Low Reynolds Numbers," *Physics of Fluids*, Vol. 26, No. 11, 2014, Paper 115107. <https://doi.org/10.1063/1.4901969>
- [35] Simoni, D., Lengani, D., Ubaldi, M., Zunino, P., and Dellacasagrande, M., "Inspection of the Dynamic Properties of Laminar Separation Bubbles: Free-Stream Turbulence Intensity Effects for Different Reynolds Numbers," *Experiments in Fluids*, Vol. 58, No. 6, April 2017, p. 66. <https://doi.org/10.1007/s00348-017-2353-7>
- [36] Alam, M. M., Zhou, Y., Yang, H. X., Guo, H., and Mi, J., "The Ultra-Low Reynolds Number Airfoil Wake," *Experiments in Fluids*, Vol. 48, No. 1, Jan. 2010, pp. 81–103. <https://doi.org/10.1007/s00348-009-0713-7>
- [37] Hoarau, Y., Braza, M., Ventikos, Y., Faghani, D., and Tzabiras, G., "Organized Modes and the Three-Dimensional Transition to Turbulence in the Incompressible Flow Around a NACA0012 Wing," *Journal of Fluid Mechanics*, Vol. 496, Dec. 2003, pp. 63–72. <https://doi.org/10.1017/S0022112003006530>
- [38] Winant, C. D., and Browand, F. K., "Vortex Pairing: The Mechanism of Turbulent Mixing-Layer Growth at Moderate Reynolds Number," *Journal of Fluid Mechanics*, Vol. 63, No. 2, 1974, pp. 237–255. <https://doi.org/10.1017/S0022112074001121>
- [39] Michalke, A., "The Instability of Free Shear Layers," *Progress in Aerospace Sciences*, Vol. 12, Jan. 1972, pp. 213–216. [https://doi.org/10.1016/0376-0421\(72\)90005-X](https://doi.org/10.1016/0376-0421(72)90005-X)
- [40] Roberts, W. B., "Calculation of Laminar Separation Bubbles and Their Effect on Airfoil Performance," *AIAA Journal*, Vol. 18, No. 1, Jan. 1980, pp. 25–31. <https://doi.org/10.2514/3.50726>
- [41] Kurelek, J. W., Lambert, A. R., and Yarusevych, S., "Coherent Structures in the Transition Process of a Laminar Separation Bubble," *AIAA Journal*, Vol. 54, No. 8, Aug. 2016, pp. 2295–2309. <https://doi.org/10.2514/1.J054820>
- [42] Roshko, A., "On the Development of Turbulent Wakes from Vortex Streets," NACA TN-2913, March 1953.
- [43] Morkovin, M., "Flow Around Circular Cylinders-A Kaleidoscope of Challenging Fluid Phenomena," *Proceedings of ASME Symposium on Fully Separated Flows*, Philadelphia, May 1964, pp. 102–118.
- [44] Roshko, A., "Structure of Turbulent Shear Flows-A New Look," *AIAA Journal*, Vol. 14, No. 10, Oct. 1976, pp. 1349–1357. <https://doi.org/10.2514/3.61477>
- [45] Dovgal, A. V., Kozlov, V. V., and Michalke, A., "Laminar Boundary Layer Separation: Instability and Associated Phenomena," *Progress in Aerospace Sciences*, Vol. 30, No. 1, 1994, pp. 61–94. [https://doi.org/10.1016/0376-0421\(94\)90003-5](https://doi.org/10.1016/0376-0421(94)90003-5)
- [46] Rist, U., "On Instabilities and Transition in Laminar Separation Bubbles, Institut für Aerodynamik & Gasdynamik, Univ. Stuttgart, Stuttgart, Germany, 2002, [https://www.iag.uni-stuttgart.de/dateien/pdf/rist\\_papers/RistTRA3Paper.pdf](https://www.iag.uni-stuttgart.de/dateien/pdf/rist_papers/RistTRA3Paper.pdf).
- [47] Yarusevych, S., Sullivan, P. E., and Kawall, J. G., "On Vortex Shedding from an Airfoil in Low-Reynolds-Number Flows," *Journal of Fluid Mechanics*, Vol. 632, Aug. 2009, pp. 245–271. <https://doi.org/10.1017/S0022112009007058>
- [48] Ripley, M. D., and Pauley, L. L., "The Unsteady Structure of Two-Dimensional Steady Laminar Separation," *Physics of Fluids A: Fluid Dynamics*, Vol. 5, No. 12, 1993, pp. 3099–3106. <https://doi.org/10.1063/1.858719>
- [49] Hunt, J. C. R., "Developments in Computational Modelling of Turbulent Flows," *Proceedings of ERCOFTAC Workshop on Numerical Simulation of Unsteady Flows and Transition to Turbulence*, EPFL, Lausanne, Switzerland, 1990, Chaps. 1, 2.
- [50] Dovgal, A. V., and Sorokin, A. M., "Instability of a Laminar Separation Bubble to Vortex Shedding," *Thermophysics and Aeromechanics*, Vol. 8, No. 2, 2001, pp. 179–186.
- [51] McGhee, R. J., and Walker, B. S., "Experimental Results for the Eppler 387 Airfoil at Low Reynolds Numbers in the Langley Low-Turbulence Pressure Tunnel," NASA TM-4062, 1988.
- [52] Althaus, D., "Profilpolaren Für Den Modellflug: Windkanalmessungen an Profilen Im Kritischen Reynoldszahlbereich," Neckar-Verlag VS-Villingen, 1980.
- [53] Volkers, D. F., "Preliminary Results of Windtunnel Measurements on Some Airfoil Sections at Reynolds Numbers Between  $0.6 \times 10^5$  and  $5.0 \times 10^5$ ," Technische Hogeschool Delft, Vliegtuigbouwkunde Memorandum M-276, 1977.
- [54] Selig, M. S., *Summary of Low Speed Airfoil Data*, Soartech Publ., Virginia Beach, VA, 1995, Appendix B.
- [55] Selig, M., Deters, R., and Williamson, G., "Wind Tunnel Testing Airfoils at Low Reynolds Numbers," *49th AIAA Aerospace Sciences Meeting*, AIAA Paper 2011-0875, Jan. 2011. <https://doi.org/10.2514/6.2011-875>
- [56] Cole, G. M., and Mueller, T. J., "Experimental Measurements of the Laminar Separation Bubble on an Eppler 387 Airfoil at Low Reynolds Numbers," NASA CR-186263, 1990.
- [57] Nichols, R. H., and Buning, P. G., *User's Manual for OVERFLOW 2.2o*, NASA Langley Research Center, March 2019, Chap. 1.
- [58] Pulliam, T. H., "High Order Accurate Finite-Difference Methods: As Seen in OVERFLOW," *20th AIAA Computational Fluid Dynamics Conference*, AIAA Paper 2011-3851, June 2011. <https://doi.org/10.2514/6.2011-3851>
- [59] Nichols, R. H., Tramel, R. W., and Buning, P. G., "Evaluation of Two High-Order Weighted Essentially Nonoscillatory Schemes," *AIAA Journal*, Vol. 46, No. 12, Dec. 2008, pp. 3090–3102. <https://doi.org/10.2514/1.36849>
- [60] Pulliam, T. H., "Time Accuracy and the Use of Implicit Methods," *11th AIAA Computational Fluid Dynamics Conference*, AIAA Paper 1993-3360, July 1993. <https://doi.org/10.2514/6.1993-3360>
- [61] Venkateswaran, S., and Merkle, C. L., "Dual Time Stepping and Preconditioning for Unsteady Computations," *33rd Aerospace Sciences Meeting and Exhibit*, AIAA Paper 1995-0078, Jan. 1995. <https://doi.org/10.2514/6.1995-78>
- [62] Pandya, S., Venkateswaran, S., and Pulliam, T. H., "Implementation of Preconditioned Dual-Time Procedures in OVERFLOW," *AIAA 41st Aerospace Sciences Meeting*, AIAA Paper 2003-0072, Jan. 2003. <https://doi.org/10.2514/6.2003-72>
- [63] Kunz, P. J., and Kroo, I., "Analysis and Design of Airfoils for Use at Ultra-Low Reynolds Numbers," *Fixed and Flapping Wing Aerodynamics for Micro Air Vehicle Applications*, edited by T. J. Mueller, Progress in Astronautics and Aeronautics, AIAA, Washington, DC, 2001, pp. 35–59. <https://doi.org/10.2514/5.9781600866654.0035.0060>
- [64] Spalart, P. R., "Strategies for Turbulence Modelling and Simulations," *International Journal of Heat and Fluid Flow*, Vol. 21, No. 3, Feb. 2000, pp. 252–263. [https://doi.org/10.1016/S0142-727X\(00\)00007-2](https://doi.org/10.1016/S0142-727X(00)00007-2)
- [65] Buning, P. G., and Pulliam, T. H., "Near-Body Grid Adaption for Overset Grids," *AIAA Aviation, 46th AIAA Fluid Dynamics Conference*, AIAA Paper 2016-3326, June 2016. <https://doi.org/10.2514/6.2016-3326>
- [66] Chan, W. M., Rogers, S. E., Nash, S. M., Buning, P. G., Meakin, R. L., Boger, D. A., and Pandya, S., *Chimera Grid Tools User's Manual, Version 2.0*, NASA Ames Research Center, 2007, Chap. 1.
- [67] Rumsey, C. L., Slotnick, J. P., and Sclafani, A. J., "Overview and Summary of the Third AIAA High Lift Prediction Workshop," *AIAA Aerospace Sciences Meeting*, AIAA Paper 2018-1258, 2018. <https://doi.org/10.2514/6.2018-1258>
- [68] Koning, W. J. F., Johnson, W., and Grip, H., "Improved Mars Helicopter Aerodynamic Rotor Model for Comprehensive Analyses," *44th European Rotorcraft Forum*, Assoc. of Aeronautical Engineers, The Netherlands, Sept. 2018, <https://www.erf2018.org/#fh5co-services>.
- [69] Koning, W. J. F., Johnson, W., and Grip, H. F., "Improved Mars Helicopter Aerodynamic Rotor Model for Comprehensive Analyses," *AIAA Journal*, Vol. 57, No. 9, Jul. 2019, pp. 3969–3979. <https://doi.org/10.2514/1.J058045>
- [70] Sahin, M., Hall, J., Mohseni, K., and Hillewaert, K., "Direct Numerical Simulation of Separated Low-Reynolds Number Flows Around an Eppler 387 Airfoil," *46th AIAA Aerospace Sciences Meeting and Exhibit*, AIAA Paper 2008-0422, Jan. 2008. <https://doi.org/10.2514/6.2008-422>
- [71] Jones, L. E., and Sandberg, R. D., "Numerical Analysis of Tonal Airfoil Self-Noise and Acoustic Feedback-Loops," *Journal of Sound and*

- Vibration*, Vol. 330, No. 25, July 2011, pp. 6137–6152.  
<https://doi.org/10.1016/j.jsv.2011.07.009>
- [72] Marxen, O., and Rist, U., “Mean Flow Deformation in a Laminar Separation Bubble: Separation and Stability Characteristics,” *Journal of Fluid Mechanics*, Vol. 660, Oct. 2010, pp. 37–54.  
<https://doi.org/10.1017/S0022112010001047>
- [73] Koning, W. J. F., Romander, E. A., and Johnson, W., “Optimization of Low Reynolds Number Airfoils for Martian Rotor Applications Using an Evolutionary Algorithm,” *AIAA Scitech 2020 Forum, AIAA-JSASS Joint Session on Martian Aerodynamics (Invited)*, AIAA Paper 2020-0084, Jan. 2020.  
<https://doi.org/10.2514/6.2020-0084>